AN EXPRESSIVE QUANTUM-DRIVEN GRAPH LEARNING APPROACH WITH APPLICATION TO MIXED-INTEGER LINEAR PROGRAMMING

Anonymous authors
Paper under double-blind review

ABSTRACT

Graph-structure data is ubiquitous, and graph learning models have recently been further extended to address complex problems like mixed-integer linear programming (MILP). However, recent literature has shown that classic graph neural networks (GNNs) suffer fundamental limitations in learning MILP graph representation, i.e., GNNs may map two different MILP graphs to the same representation. To overcome the limitations of classical GNNs, we introduce an expressive quantum-driven graph learning approach, leveraging quantum machine learning (QML) to recognize patterns that are difficult for classical methods to learn. Specifically, the proposed versatile quantum graph learning architecture, composed of a node feature layer, a graph message interaction layer, and an optional auxiliary layer. Its versatility is reflected in effectively encoding features of nodes and edges while ensuring node permutation equivariance and flexibly creating different circuit structures for various expressive requirements and downstream tasks. VQGLA is well suited for learning complex graph tasks like MILP representation. Experimental results highlight the effectiveness of VQGLA in capturing and learning representations for MILPs. In comparison to traditional GNNs, VQGLA exhibits superior discriminative capabilities and demonstrates enhanced generalization across various problem instances, making it a more promising solution for complex optimization tasks.

1 INTRODUCTION

Mixed-integer linear programming (MILP) serves as a general optimization formulation applicable to diverse real-world optimization scenarios, such as transportation (Schouwenaars et al., 2001), scheduling (Floudas & Lin, 2005b), and production planning (Askari-Nasab et al., 2011). MILP aims to minimize a linear objective function while adhering to linear constraints. Apart from the classic non-learning solvers that often resort to heuristics, recent learning-based models have been actively studied, and graph neural networks (GNNs) are considered a suitable backbone to represent the mappings for MILP instances in various stages of MILP solving processes (Khalil et al., 2022; Gupta et al., 2022; Wang et al., 2023). A MILP instance can be regarded as a weighted bipartite graph with node features, as illustrated in Fig. 1 and Fig. 2. Due to the beneficial property of GNN, permutations on variables or constraints of a MILP do not essentially change the problem itself. This can prevent the model from overfitting the variable/constraint orders in the training data. However, a recent study (Chen et al., 2023) revealed that the classical GNNs based on the message-passing mechanism suffer fundamental limitations in graph representation, especially for MILP graphs, *i.e.*, GNNs do not have sufficient

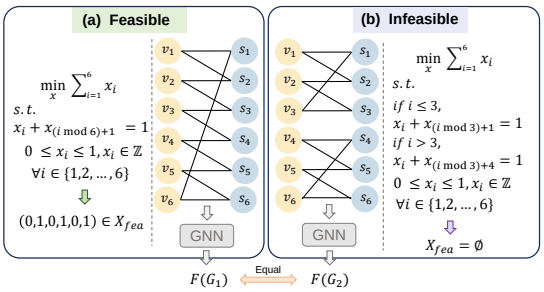

Figure 1: A pair of *GNN-intractable* MILPs G_1 and G_2. **(a)** is feasible and **(b)** is infeasible. Although their edge connectivity and feasibility are different, GNNs embed them into the same representation.

Table 1: Comparison of QNNs for *classical* graph data on several aspects: whether the models provide implementable circuits, enjoy permutation equivariance, consider multi-dimensional node or edge features, utilize quantum (Q) layers or classical (C) layers, and the manner of readout. Compared to other methods, our proposed model addresses multiple aspects, can be applied to both node-level and graph-level tasks, and achieves advantage validation over GNNs in learning graph representations.

Method	Quantum Circuit Embodied	Permutation Equivariance	Attribute	Layer	Readout	Application
QGNN (Verdon et al., 2019)	✗	✓	—	Q	Tomography	Learning Hamiltonian Dynamics & Graph Isomorphism Classification
QGCN (Zheng et al., 2021)	✓	✗	Node & Edge	Q	Estimation	Image Classification
egoQGNN (Ai et al., 2022)	✓	✗	Node	Q & C	Tomography	Graph Classification
EQGC (Mernyei et al., 2022)	✗	✓	Node	Q & C	Estimation	Synthetic Cycle Graph Classification
Ours	✓	✓	Node & Edge	Q	Estimation	Graph Classification & Regression

power to distinguish some different instances. Specifically, as shown in Fig. 1, two different MILP instances can be eventually embedded into the identical representation by GNNs, thus failing to predict the feasibility of MILP. Moreover, in real-world scenarios, there are numerous MILPs that GNNs cannot distiguish (Chen et al., 2023), which means that practitioners using GNNs may not benefit from this.

As we can see, classical GNNs face fundamental limitations in learning graph representation. To overcome this challenge, we turn to quantum machine learning (QML), which is an emerging field that combines the power of quantum computing with the capabilities of machine learning. QML has shown immense potential in recent years, such as recognizing patterns that are intractable using classical methods (Biamonte et al., 2017). In this paper, we aim to associate nodes with qubits and edges with quantum entanglement, investigating graph structures that are indistinguishable from classical GNNs and exploring effective approaches for constructing quantum graph neural networks.

Designing a quantum learning framework for unstructured data, such as graph data, is still in its nascent stages. Although some quantum neural networks (Verdon et al., 2019; Zheng et al., 2021; Ai et al., 2022; Mernyei et al., 2022) designed to handle graph data have been proposed, they struggle to effectively apply to complex graph tasks such as MILP graphs because they fail to address the following challenges simultaneously. **i)** Since complex graph data usually contains node and edge features, it is important to design a reasonable node/edge feature encoding strategy that enables the quantum circuit to utilize these features to learn effective node representations.**ii)** As mentioned earlier, classic GNNs possess the beneficial property of *permutation equivariance*. However, designing a quantum circuit that conforms to permutation equivariance is nontrivial and requires careful design. **iii)** Unlike building hybrid classical-quantum layers, designing full quantum circuits for classical graph data and verifying them in practical graph tasks is challenging. Moreover, we provide a detailed discussion of related works in Appendix A and Table 1 here as a summary.

To tackle the above challenges, we propose a **versatile quantum graph learning architecture named VQGLA**. This method aims to provide a quantum solution for complex graph tasks like learning MILP representation and to demonstrate superior discriminative power over classical GNNs. The versatility of VQGLA is reflected in the following five aspects. **i)** VQGLA can encode node and edge features. We design learnable features associated with each feature and flexible encoding schemes to better learn node representations. **ii)** With the proposed parameter-sharing strategy, all the layers in VQGLA possess the beneficial property of permutation equivariance, and we provide the theoretical proof in Sec. 4.3. **iii)** VQGLA can incorporate an optional auxiliary layer to enhance the expressive power of the model. **iv)** The types of quantum gates in VQGLA are adjustable under our configuration principle, allowing flexible use across different scenarios. **v)** By designing different measurement layers, VQGLA can be applied to graph tasks at various levels, such as graph classification, graph regression, and node property prediction. **We summarize the main contributions:**

1) To explore the potential of quantum machine learning for learning graph-structured data, we present a versatile quantum graph learning architecture (VQGLA). The method is based on fully quantum circuits compatible with current devices and is capable of effectively encoding the features of nodes and edges while ensuring node permutation equivariance. VQGLA can flexibly create different circuit structures to meet various expressive requirements and downstream tasks. Moreover, we theoretically prove the permutation equivariance of VQGLA.

2) We implement VQGLA in an application for learning MILP representation, which is evaluated on three tasks: predicting feasibility, the optimal value, and the optimal solution. Numerical experiments

demonstrate the advantage of VQGLA over classic GNNs in learning MILP representations. VQGLA has better discriminative power to handle GNN-intractable MILPs. It also shows that VQGLA has better generalization and uses fewer parameters.

3) The superior discriminative power of VQGLA over GNNs not only provides a promising solution for handling more challenging graph tasks but also offers positive support for the capacity of quantum machine learning methods. This will encourage further exploration of the potential of QNNs over their classical counterparts.

2 PRELIMINARIES

We provide the basics of quantum computing and quantum machine learning in a simple and understandable way in Appendix B, ensuring that readers with a background in linear algebra but not familiar with quantum computing can gain a basic understanding of the quantum technologies used in our paper. The matrix forms of all quantum gates mentioned in the paper are provided in Table 10. Next, we will introduce the specific form of MILP graphs and the types of MILP datasets.

2.1 MILP GRAPHS AND THE LIMITATION OF CLASSIC GNNS

Graph Representation for MILPs. An instance is defined as follows $A \in \mathbb{R}^{p\times q}$, $b \in \mathbb{R}^p$, $c \in \mathbb{R}^q$:

$$\min_{x\in\mathbb{R}^q} \; c^\top x, \quad \text{s.t.} \;\; Ax \circ b, \;\; l \le x \le u, \;\; x_i \in \mathbb{Z}, \; \forall\, i \in I, \tag{1}$$

where l and u represent the upper and lower bounds on variables, where $l \in (\mathbb{R} \cup \{-\infty\})^q$, $u \in (\mathbb{R} \cup \{+\infty\})^q$ and $\circ \in \{\le, =, \ge\}^p$. Consistent with Chen et al. (2023), the mathematical operators $\{\le, =, \ge\}$ are mapped into numerical value $\{0, 1, 2\}$, respectively. $I \subseteq \{1, \cdots, q\}$ represents the index set of integer variables. The *feasible solution* is defined as the set $X_{fea} = \{x \in \mathbb{R}^q \mid Ax \circ b, \; l \le x \le u, \; x_i \in \mathbb{Z}, \; \forall i \in I\}$, while $X_{fea} = \emptyset$ means the MILP problem is *infeasible*. Feasible MILPs have an *optimal objective value* $y_{obj} = \inf\{c^\top x \mid x \in X_{fea}\}$. If there exists $\hat{x} \in X_{fea}$ such that $c^\top \hat{x} \le c^\top x, \forall\, x \in X_{fea}$, then $\hat{x}$ is an *optimal solution*. Nevertheless, the optimal solution may not always exist because the optimal objective value can be arbitrarily good, where the MILP problem is *unbounded* and categorized as feasible with an optimal objective value of $-\infty$. Following the protocol in Gasse et al. (2019) and Chen et al. (2023), we formulate MILP as a *weighted bipartite graph* to interpret variable-constraint relationships, as illustrated in Fig. 2. The vertex set is $V \cup S$, where $V = \{v_1, \cdots, v_i, \cdots, v_q\}$ with v_i representing the i-th variable and $S = \{s_1, \cdots, s_j, \cdots, s_p\}$ with s_j representing the j-th constraint. The edge connected v_i and s_j has weight $A_{i,j}$. Based on Eq. (1), the vertex $v_i \in V$ is associated with a feature vector $f_i^V = (c_i, l_i, u_i, \epsilon_i)$, where $\epsilon_i \in \{0, 1\}$ represents whether variable v_i takes an integer value. The vertex s_j is equipped with a two-dimensional vector $f_j^S = (b_j, \circ_j)$. There is no edge between vertices in the same vertex set (V or S). The weighted bipartite graph with node features is named an *MILP-induced graph* or *MILP graph*.

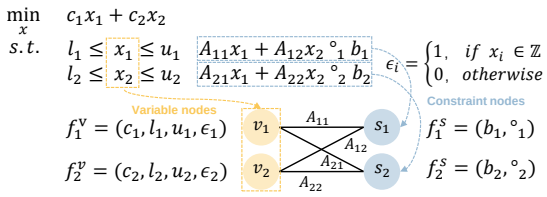

Figure 2: A weighted bipartite graph of a MILP instance. v_i is the variable node associated with feature f_i^V and s_j indicates the constraint node associated with feature f_j^S. The edge between v_i and s_j means the j-th constraint involves the i-th variable.

Classic GNNs may Fail on General MILPs. Recall that Chen et al. (2023) has shown that GNNs may embed two different (one feasible and one not) MILPs into an identical embedding. In fact, there are infinitely many pairs of MILP instances that can puzzle GNNs. Therefore, Chen et al. (2023) call this class of MILPs that confuse GNNs as *foldable* MILPs, while the rest of the MILPs are named *unfoldable* MILPs. In this paper, we refer to them as *GNN-intractable* MILPs and *GNN-tractable* MILPs, respectively. Fig. 1 gives an example of a pair of MILPs in the GNN-intractable MILP dataset. In this case, $f_i^V = (1, 0, 1, 1)$, for all $v_i \in V$ and $f_j^S = (1, =)$, for all $s_j \in S$. All edge weights are equal to 1, which means that the only difference between the two bipartite graphs lies in the connectivity of edges. However, these two MILP instances have different feasibility. Fig. 1 (a) is feasible, e.g. $x = (0, 1, 0, 1, 0, 1)$ is a feasible solution, while Fig. 1 (b) is infeasible as there are no integer decision variables that can satisfy the equality constraint $2(x_1 + x_2 + x_3) = 3$. Appendix E.1 illustrates why GNN has no ability to distinguish between them. The limitation of GNNs means that directly applying GNNs to represent general MILPs may fail.

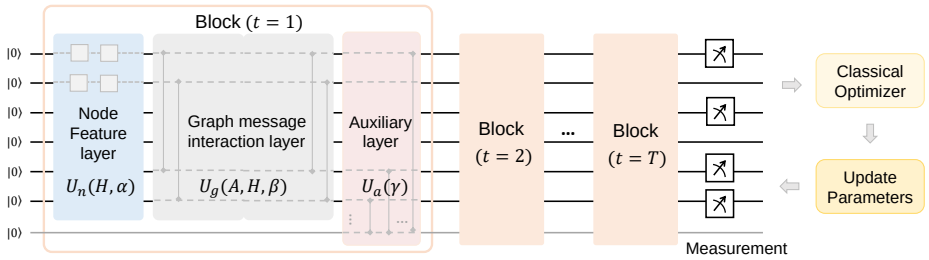

Figure 3: The overall architecture of our VQGLA. The node feature layer encodes and learns node features into the quantum circuit, and the graph message interaction layer contains a variable update layer and a constraint update layer. The auxiliary layer is optional and is used to enhance the model's capacity. All layers are designed to preserve the equivariance of the node permutation.

Remark. Quantum machine learning is still in its infancy, especially quantum graph machine learning. VQGLA can be regarded as the *most basic* graph neural network in the field of quantum computing. We aim for VQGLA to play a similar foundational role in quantum graph learning as message-passing GNNs do in classical graph learning.

3 Versatile Quantum Graph Learning Architecture

Fig. 3 shows the overall framework of VQGLA, which consists of the node feature layer, graph message interaction layer, auxiliary layer, and measurement layer. The first three layers form a block. After the block is iteratively repeated Γ times, Pauli-Z measurement is performed. This section introduces the design details of each layer in VQGLA using MILP graphs as an example. The next section presents how VQGLA can be applied to various levels of graph tasks of MILP and demonstrates its permutation equivariance and discriminative power.

3.1 Node Feature Layer

Fig. 4 (a) exemplifies a node feature layer with two variable nodes and two constraint nodes. The variable nodes v_i have four features $(c_i, l_i, u_i, \epsilon_i)$, and the constraint nodes s_j have two features $(b_j, \circ_j)$. Suppose that each qubit encodes two features, as shown in Fig. 4 (c). Specifically, $W(\theta)$ and $D(\theta)$ represent two *different* types of single-qubit quantum gates, including $\{R_X(\theta), R_Y(\theta), R_Z(\theta)\}$, where θ indicates the parameter of the gate. We can set θ as either trainable parameters or a constant that need to be encoded. The selection principle of single-qubit quantum gates ($W(\theta)$ and $D(\theta)$) will be described in Sec. 3.4. In this case, the first qubit encodes the features c_1 and l_1, and the second qubit encodes the features u_1 and ϵ_1. That is, the first two qubits are used to represent the node v_1. When fewer features are encoded on each qubit, more qubits are used to represent a node, resulting in a richer node representation. However, this also leads to increased model complexity, so we set ω as a hyperparameter to denote the maximum number of features that each qubit can encode, balancing the speed and accuracy of the model. Fig. 4 shows the situation where $\omega = 2$, and we also provide another illustration of $\omega = 4$ in Fig. 8 in the Appendix. Moreover, the same feature dimension (*e.g.*, c_1 and c_2) shares the identical *trainable* parameter (*i.e.*, $\alpha_{t,1}$ in the $W(c_1 + \alpha_{t,1})$ and $W(c_2 + \alpha_{t,1})$). In other words, the trainable parameters are related only to the feature dimension, not to the permutation of the nodes. Thereby, even if the order of nodes changes (*e.g.*, encoding node v_2 using the first two qubits), each node's features are assigned the same trainable parameters, ensuring that the learned node feature representation remains invariant. In this way, the node feature layer can preserve the node permutation equivariance, see Sec. 4.3 for proof. The node feature layer encodes all variable features $\mathrm{H}^{\mathrm{V}} \in \mathbb{R}^{\mathrm{q}\times 4}$ and constraint features $\mathrm{H}^{\mathrm{S}} \in \mathbb{R}^{\mathrm{p}\times 2}$ can be defined as:

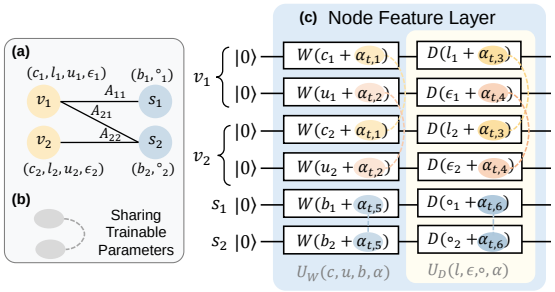

Figure 4: Node features are encoded into the circuit using angle encoding, and each feature is associated with a trainable parameter to learn the node representation. For node permutation equivariance, the same feature dimension (*e.g.*, c_1 and c_2) shares the identical trainable parameter (*i.e.*, $\alpha_{t,1}$).

$$U_x(H, \alpha_t) = U_W(c, u, b, \alpha_t) U_D(l, \epsilon, \circ, \alpha_t), \tag{2}$$

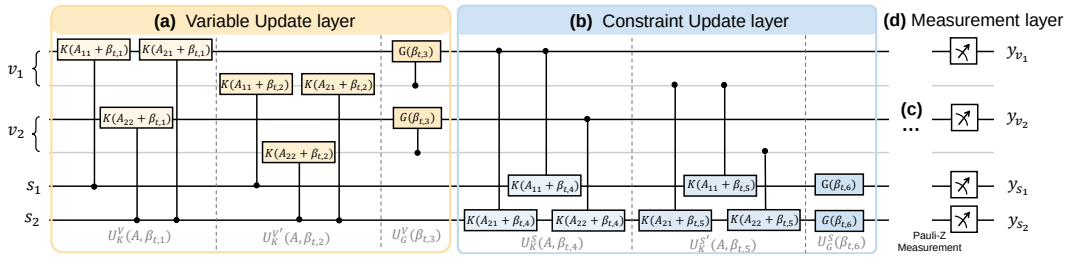

Figure 5: The quantum graph message interaction layer. **(a)** Variable update layer. Controlled-K gates are used to learn the information interaction between variable nodes and constraint nodes, while controlled-$G(\theta)$ gates are utilized to learn the internal interaction between qubits representing the same variable nodes. **(b)** Constraint update layer. Controlled-K gates are turned upside down and are followed by $G(\theta)$ gates to update the representation of constraint nodes. **(c)** Omitted node feature layers and graph message interaction layers. **(d)** Measurement layer using Pauli-Z measurement.

3.2 Quantum Graph Message Interaction Layer

We employ two-qubit quantum gates to entangle the qubits representing two nodes connected by an edge. By harnessing the mechanism of quantum entanglement, we can learn the information interaction in MILP graphs. Fig. 5 exemplifies the graph message interaction layer for the MILP graph in Fig. 4 (a), which contains three edges. Specifically, this layer includes two parts: the variable update layer and the constraint update layer. We set the two-qubit quantum gates as controlled-$K(\theta) \in \{R_X(\theta), R_Y(\theta), R_Z(\theta)\}$. In the variable update layer, the control qubit of controlled-$K(\theta)$ gate is the constraint node, and its target qubit is the variable node. Different edges share an identical trainable parameter β_t, as illustrated in the first three gates in Fig. 5 (a). In this case, one variable node is represented by two qubits. Interestingly, the order of controlled-K gates can be arbitrary due to the character of bipartite graphs, *i.e.*, whether the controlled-$K(A_{11} + \beta)$ or the controlled-$K(A_{22} + \beta)$ is applied first does not change the unitary of the $U_K^{\cdot}$ layer. We refer to this property as *edge permutation invariance*. In the MILP graph, the edge feature is the edge weight, but VQGLA can also be applied to cases with multi-dimensional edge features, as illustrated in Fig. 9 in the Appendix. Moreover, the controlled-G gate is applied to these two qubits to learn the interaction of *internal* information within one node, where controlled-$G(\theta) \in \{CR_X(\theta), CR_Y(\theta), CR_Z(\theta)\}$. In the constraint update layer, the controlled-K gates are turned upside down and are followed by $G(\theta)$ gates to update the feature representation of constraint nodes. The selection principle of K and G gates will be described in Sec. 3.4. The unitary of the t-th graph message interaction layer can be represented by $U_g(A, \beta_t) = U_{gv}(A, \beta_t) \cdot U_{gs}(A, \beta_t)$, with formulas shown in Eq. 8. We also provide a simple and intuitive explanation in Appendix D.2.4. Furthermore, we theoretically prove the node permutation invariance of this layer in Sec. 4.3.

3.3 Auxiliary Layer

To further enhance the expressiveness of the model, inspired by Wu et al. (2021), we introduce an optional auxiliary layer, which can facilitate the interaction of information within the graph. Specifically, each auxiliary qubit is connected to all other nodes through symmetric two-qubit gates $R_{ZZ}(\gamma)$. In this way, the model can increase the width and number of parameters. For the two qubits representing one variable, trainable parameters $\gamma_{t,1}$ and $\gamma_{t,2}$ are assigned, while the parameter $\gamma_{t,3}$ is assigned to the qubit representing constraints. The unitary of the auxiliary layer is defined as $U_a(\gamma_t)$. We can choose a varying number of auxiliary qubits based on the requirements of different tasks. The node feature layer, graph message interaction layer, and auxiliary layer are regarded as a block. After iterating this block Γ times, the unitary matrix of the overall circuit is equal to

$$U_{qgl}(A, H, \Theta) = \prod_{t=1}^{\Gamma} U_x(H, \alpha_t) U_g(A, \beta_t) U_a(\gamma_t), \tag{3}$$

where Θ contains all trainable parameters α, β, and γ.

3.4 Configuration Principle of VQGLA

In VQGLA, the quantum gates $W(\theta)$, $D(\theta)$, $K(\theta)$, and $G(\theta)$ are selected from $\{R_X(\theta), R_Y(\theta), R_Z(\theta)\} = \{\exp(-\mathbf{i}\theta\sigma_x), \exp(-\mathbf{i}\theta\sigma_y), \exp(-\mathbf{i}\theta\sigma_z)\}$, where $\{\sigma_x, \sigma_y, \sigma_z\}$ are Pauli matrices form a basis for the real vector space of 2×2 Hermitian matrices. $\{\mathbf{i}\sigma_x, \mathbf{i}\sigma_y, \mathbf{i}\sigma_z\}$ form a basis for the real Lie algebra $\mathfrak{su}(2)$, which exponentiates to the special unitary group $SU(2)$. When two quantum gates

are adjacent in VQGLA, they are expected to be of different types. This enables the encoding of various features or trainable parameters on different bases, thereby enriching the information encoded in the circuit and preventing the quantum circuit from confusing different features. There are six possible configurations of VQGLA, which are summarized in Table 11.

4 VQGLA WITH APPLICATION TO MILP

As the application of VQGLA, predicting feasibility, optimal objective value, and optimal solution of MILP graphs can be regarded as the task of graph classification, graph regression, and node property prediction, respectively. As we can see, learning the MILP representation is a sufficiently complex task that fully utilizes VQGLA, thereby comprehensively showcasing its capabilities.

4.1 MEASUREMENT LAYER

As shown in Fig. 5 (d), we add a measurement layer at the end of the quantum circuit. After the measurement operation, the quantum information can be translated into classical information. In the measurement layer, we measure only the first qubit representing each node using Pauli-Z measurement. That is, for q variable nodes and p constraint nodes, VQGLA outputs $q+p$ results. The output of the VQGLA is defined as $\Phi(A, H, \Theta) = \{\langle 0|U^{\dagger}_{qgl}(A, H, \Theta)O_i U_{qgl}(A, H, \Theta)|0\rangle\}_{i=1}^{q+p}$, where O_i represents i-th observable. For predicting the feasibility and optimal value of MILP graphs, we define $\phi_{\text{fea}}(A, H) = \sum_{i=1}^{q+p} \Phi(A, H, \Theta_{fea})_i$, $\phi_{\text{obj}}(A, H) = \sum_{i=1}^{q+p} \Phi(A, H, \Theta_{obj})_i$. For predicting the optimal solution, we define $\phi_{\text{sol}}(A, H) = \{\Phi(A, H, \Theta_{sol})_i\}_{i=1}^{q}$. As can be seen, the three tasks use the same circuit structure of VQGLA but employ different trainable parameters and different ways to utilize the information obtained by measurements.

4.2 TRAINING AND TESTING

For predicting the feasibility, $\hat{y}_{fea} = \phi_{\text{fea}}(A, H)$, we utilize the negative log-likelihood as the loss to train VQGLA. In the testing, we set an indicator function $\mathbb{I}_{\hat{y}_{fea}>1/2}$ to calculate the *error rate*: $\frac{1}{M}(\sum_{m=1}^{M} y^m_{fea} \cdot \mathbb{I}^m_{\hat{y}_{fea}>1/2})$, where M indicates the number of tested MILP instances, to evaluate the number of correct predictions for feasibility.

For predicting the optimal solutions, $\hat{y}_{sol} = \lambda\phi_{\text{sol}}(A, H)$, where λ is the maximum range of variables of the training sample, *i.e.*, $\max\{\{\{abs(l^e_i), abs(u^e_i)\}_{i=1}^{q}\}_{e=1}^{E}\}$. We use the *mean square error* as the training and testing metric: $\frac{1}{Mq}\sum_{m=0}^{M-1} \|y_{sol} - \hat{y}^m_{sol}\|^2_2$, where y^m_{sol} is the ground truth.

For predicting the optimal values, $\hat{y}_{obj} = \delta\lambda\phi_{\text{obj}}(A, H)$, where $\delta = \max\{\{\{c^e_i\}_{i=1}^{q}\}_{e=1}^{E}\}$ is the maximum range of coefficients of training sample. We also use the *mean square error* to train or evaluate, *i.e.*, $\frac{1}{M}\sum_{m=0}^{M-1}(y^m_{obj} - \hat{y}^m_{obj})^2$.

4.3 PERMUTATION EQUIVARIANCE AND INVARIANCE

Permutation equivariance and invariance are fundamental requirements for graph neural networks. In this section, we will demonstrate that the proposed quantum graph learning architecture possesses these desirable properties. Let $G = (A, \mathrm{H}^{\mathrm{V}}, \mathrm{H}^{\mathrm{S}})$ represent a MILP graph with q variable nodes and p constraint nodes. π_q and π_p are the permutations of variable nodes and constraint nodes, respectively. $\Lambda_q \in \mathbb{B}^{q\times q}$ and $\Lambda_p \in \mathbb{B}^{p\times p}$ are permutation matrices representing a permutation π_q and π_p, respectively. Additionally, we define a permutation π_{q+p} on the $(q+p)$ elements to indicate the overall permutation on all nodes of the MILP graph. Λ_{q+p} is the permutation matrix of the permutation π_{q+p}. $\widetilde{\Lambda}$ is the *unitary* representation of π_{q+p}, which indicates the permutation of qubits representing nodes. Based on this, we give the definition of a permutation equivariant circuit.

Defintion 1. ***(Permutation Equivariant Circuit).*** *A parameterized quantum circuit U is permutation equivariant for MILP graphs (A, H^V, H^S) if it satisfies*

$$U(\Lambda_p A \Lambda_q, \Lambda_q H^V, \Lambda_p H^S, \Theta) = \widetilde{\Lambda}^{\dagger} \cdot U(A, H^V, H^S, \Theta) \cdot \widetilde{\Lambda}. \tag{4}$$

Appendix D.1 provides the formulation and detailed explanation of Definition 1. After measuring the quantum circuit, we can consider the model to be a mapping $\phi \in \mathbb{R}^{q+p}$. According to Definition 1, we can obtain the permutation equivariance of the mapping.

Defintion 2. ***(Permutation Equivariant Mapping).*** *A mapping $\phi(\cdot) \in \mathbb{R}^{q+p}$ is permutation equivariant for MILP graphs (A, H^V, H^S) if it satisfies*

$$\phi(\Lambda_p A \Lambda_q, \Lambda_q H^V, \Lambda_p H^S) = \Lambda_{q+p} \cdot \phi(A, H^V, H^S).$$

It indicates that the mapping result after node permutation $\phi(\Lambda_p A \Lambda_q, \Lambda_q \mathrm{H}^{\mathrm{V}})$ is equal to the result of applying the permutation π_{q+p} to the original result $\phi(A, \mathrm{H}^{\mathrm{V}}, \mathrm{H}^{\mathrm{S}})$. In addition, we can aggregate the result of the permutation equivariant mapping as a value to obtain the other mapping $\kappa \in \mathbb{R}$. The mapping is permutation invariant if changing the order of inputs does not alter the mapping output.

Defintion 3. ***(Permutation Invariant Mapping).*** *A mapping $\kappa(\cdot) \in \mathbb{R}$ is permutation invariant for MILP graphs if it satisfies*

$$\kappa(\Lambda_p A \Lambda_q, \Lambda_q H^V, \Lambda_p H^S) = \kappa(A, H^V, H^S).$$

Theorem 1. *In the proposed VQGLA, the circuit $U_{peqg}(A, H^V, H^S, \Theta)$ is a permutation equivariant circuit. After Pauli-Z measurement, the output of the circuit $\Phi(A, H, \Theta_{sol}) = \phi_{sol}(A, H)$ is a permutation equivariant mapping. $\phi_{fea}(A, H) = \sum_{i=1}^{q+p} \Phi(A, H, \Theta_{fea})_i$ and $\phi_{obj}(A, H) = \sum_{i=1}^{q+p} \Phi(A, H, \Theta_{obj})_i$ are permutation invariant mapping.*

Appendix D.2 provides a detailed proof of Theorem 1, offering theoretical guarantees of permutation equivariance and invariance for our proposed VQGLA.

4.4 Superior Discriminative Power over GNNs

As mentioned earlier, Chen et al. (2023) have shown that GNNs may fail to distinguish two MILP graphs, which is because of the fundamental limitations of GNNs. Xu et al. (2018) have shown that GNNs are **at most** as powerful as the Weisfeiler-Lehman (WL) test (Weisfeiler & Leman, 1968) in distinguishing graph structures. However, as the WL test iteratively updates the label of vertices in a graph only based on the label of their neighboring vertices, if two graphs exhibit subtle structural differences not reflected in the degree of vertices or the patterns of local neighbors, the WL test will fail to distinguish between these two graphs, as shown in Fig. 1. See Appendix E.1 for a detailed explanation of why GNN fails on the MILPs. By contrast, benefiting from quantum entanglement between nodes, VQGLA can capture the difference in edge connectivity between two MILP graphs. Different edges result in variations in graph-message interaction layer U_k, *i.e.*, $\exp(-\mathbf{i}(\sum_{(i,j)\in\mathcal{E}} A_{i,j}(I - \sigma_z)_i P^K_{q+j}))$. We give the detailed proof in Appendix E.2.

5 Experiments

In the experimental section, we compare the performance between classical GNNs and quantum machine learning algorithms on the learning representation of MILP graphs. The construction of the MILP dataset is in line with Chen et al. (2023) (see details in Appendix G). We use Adam (Kingma & Ba, 2014) with an initial learning rate of 0.1 to find the optimal parameters of VQGLA, and batch size is set at 16. Experiments are performed on a single machine with 4 2.20GHz CPUs and four NVIDIA A100 GPU. The source code is written using TorchQuantum (Wang et al., 2022a), a PyTorch-based library for quantum computing, which can simulate quantum circuits with up to 26 qubits. In Table 11 of Appendix F, the performance of all possible types of VQGLA are compared, and we finally select $(W(\theta), D(\theta), K(\theta), G(\theta)) = (R_X(\theta), R_Z(\theta), R_Y(\theta), R_Z(\theta))$ for the following experiments.

5.1 Comparison with Classical GNNs

We first compare the GNN used in Chen et al. (2023) named MILP-GNN as it is designed for MILP. Our VQGLA model has a hyperparameter to control the number of circuit parameters, *i.e.*, the number of blocks T. The number of parameters for predicting feasibility is $12 \times T$. MILP-GNN also has a hyperparameter embedding size d controlling the number of parameters. Taking predicting feasibility as an example, the number of parameters is $30d^2 + 30d$. We vary these two hyperparameters separately for evaluation. In all our experiments, we first gradually increase their embedding size or our blocks to test the performance of the models and find d^* or T^* corresponding to the best performance. Then, we select the values near d^* or T^* and show their corresponding results.

Table 2: Performance Comparison on the GNN-tractable MILP dataset.

		Feasibility (Rate of Error ↓)/10^{-2}			**Optimal Value** (MSE ↓) /10^{-2}			**Optimal Solution** (MSE ↓) /10^{-1}		
MILP-GNN (Chen et al., 2023)	**# E.Size**	**4**	**6**	**8**	**4**	**6**	**8**	**16**	**24**	**32**
	Train	6.72 ± 0.17	5.42± 0.21	4.29± 0.12	1.52± 0.04	1.12± 0.06	0.66± 0.03	7.84± 0.21	6.39± 0.26	5.47± 0.15
	Test	7.96± 0.19	6.74± 0.20	5.62± 0.11	2.35± 0.07	1.64± 0.05	1.76± 0.04	8.82± 0.27	7.57± 0.21	6.31± 0.25
VQGLA	**# Block**	**4**	**6**	**8**	**6**	**8**	**10**	**8**	**10**	**12**
	Train	7.22± 0.11	6.53± 0.13	5.57± 0.08	1.10± 0.04	1.00± 0.02	0.98± 0.01	6.10± 0.14	5.79± 0.10	5.70± 0.09
	Test	7.34± 0.12	6.65± 0.12	5.74± 0.09	1.26± 0.05	1.13± 0.03	1.11± 0.02	6.37± 0.11	6.03± 0.08	5.99± 0.07

5.1.1 Experiments on GNN-intractable MILP Dataset

GNN-intractable MILPs contain many pairs of WL indistinguishable graphs that cannot be distinguished by classic GNNs (Chen et al., 2023). Here, we randomly generate $2,000$ GNN-intractable MILPs with 12 variables and 6 constraints, and there are $1,000$ feasible MILPs while the others are infeasible. The error rate serves as the evaluation criterion for predicting the feasibility of GNN-intractable MILPs. We compare our VQGLA with the classical GNNs, *i.e.*, MILP-GNN (Chen et al., 2023) and MILP-GNN with random features. MILP-GNN with random features is proposed by Chen et al. (2023) to alleviate the limitations of the original GNN by appending random features to the MILP graphs. As shown in Fig. 6, the error rate of MILP-GNN is highest regardless of the embedding size, as it cannot distinguish GNN-intractable MILPs. Although MILP-GNN with random features can improve performance, it achieves the best when the embedding size is 32, which will cost $30,565$ parameters. Moreover, adding random features may cause additional issues, *i.e.*, changing the feasibility or solution of the original problem, resulting in the change of ground truth of the dataset. In contrast, VQGLA can capture the edge connectivity of GNN-intractable MILPs, so it can achieve accurate test results with just 4 blocks, *i.e.*, 48 parameters. The results show that VQGLA has better discriminative power than GNNs with fewer parameters.

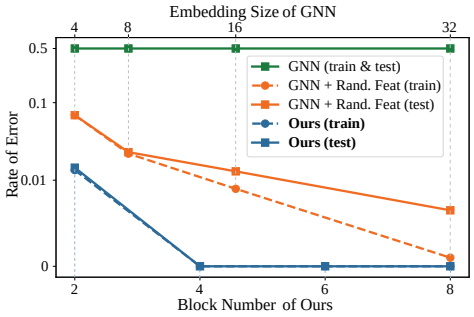

Figure 6: Comparison on GNN-intractable MILPs. *GNN* refers to MILP-GNN (Chen et al., 2023), and *GNN + Rand. feat.* indicates the MILP-GNN with random features.

5.1.2 Experiments on GNN-tractable MILP Dataset

We further compare our VQGLA and MILP-GNN on the GNN-tractable MILPs that GNNs can distinguish. We randomly generate $8,290$ GNN-tractable MILPs with four variables and four constraints, with feasible and infeasible MILPs each accounting for half. The experiments evaluate the rate of error in predicting the feasibility and the mean squared error (MSE) of predicting optimal values and optimal solutions of MILPs. As reported in Table 2, as the embedding size increases, the training error of MILP-GNN decreases, but its generalization error on the test set increases. The reason is that GNN-tractable datasets are challenging, with diverse training and test sets, making it difficult for MILP-GNN to generalize well on the test set. In contrast, our VQGLA benefits from quantum mechanisms, leading to better generalization performance.

5.1.3 Comparison with Advanced GNNs

We utilize the PyG (PyTorch Geometric) library [1] to extend more GNN models into frameworks suitable for MILP graphs. We modify each GNN to update variable nodes and constraint nodes using different weights. Table 3 compares our methods with GAT (Graph Attention Network) (Veličković et al., 2018), GATv2 (Brody et al., 2022), and Graph Transformer (Shi et al.,

Table 3: Comparison of VQGLA and other GNNs on the GNN-intractable and GNN-tractable dataset.

	Embedding Size/ # Blocks	**2**	**4**	**6**	**8**
GNN-tractable dataset	GAT	0.856	0.926	0.930	0.940
	GATv2	0.914	0.927	0.936	0.943
	Graph Transformer	0.875	0.914	0.920	0.930
	MILP-GNN	0.872	0.910	0.911	0.902
	VQGLA	0.933	0.936	0.942	0.946
GNN-intractable dataset	GAT	0.500	0.500	0.500	0.500
	GATv2	0.500	0.500	0.500	0.500
	Graph Transformer	0.500	0.500	0.500	0.500
	MILP-GNN	0.500	0.500	0.500	0.500
	VQGLA	0.987	0.998	1.000	1.000

[1] https://pytorch-geometric.readthedocs.io/en/latest/

Table 4: Comparison between different quantum models on predicting the feasibility of MILPs.

	HEA (Kandala et al., 2017)	QGCN (Zheng et al., 2021)	**VQGLA (ours)**
Train	0.4613± 0.024	0.3419± 0.015	**0.1086**± 0.008
Test	0.4665± 0.020	0.3475± 0.018	**0.1127**± 0.012

Table 5: Performance changes as the number of auxiliary qubits increases on predicting optimal solution.

# Aux. qubits	**0**	**1**	**2**	**3**
Train	0.6580	0.6166	**0.5694**	0.6099
Test	0.6853	0.6410	**0.5993**	0.6354

2021), *w.r.t* the accuracy of feasibility prediction on GNN-intractable and GNN-tractable datasets. As we can see, in the GNN-tractable dataset, our method remains competitive with advanced GNNs, achieving nearly the best results, and advanced GNNs still struggle with GNN-intractable datasets, whereas our model is more effective.

5.2 Comparison with Other Quantum Algorithms

Recall in Table 1 that most quantum GNNs have not considered edge features, which yet are vital for solving MILP. Therefore, we only compare QGNNs that consider edge features, such as the quantum graph CNN (QGCN) (Zheng et al., 2021). We also compare a problem-agnostic, hardware-efficient ansatz (HEA) (Kandala et al., 2017). The circuit structure of HEA is typically fixed, making it unable to encode the edge information of a graph, but can encode the node feature information of the graph. Table 4 reports the error rates on the GNN-tractable MILP dataset with three variables and three constraints. In this MILP dataset, QGCN requires more qubit resources to compute than our VQGLA. Moreover, we set the number of parameters for all quantum models to 96 for performance comparison. The results show that the problem-agnostic ansatz cannot effectively learn from graph data. Although QGCN is a problem-inspired ansatz and designs an equivariant graph convolution layer, their pooling layers violate permutation invariance, leading to performance degradation in predicting MILP feasibility. By contrast, VQGLA ensures the permutation invariance to achieve better performance.

5.3 Ablation Study

Table 5 investigates the contribution of auxiliary layers to VQGLA, which shows the performance of VQGLA in predicting the optimal solution with an increasing number of auxiliary qubits. The results indicate that increasing the number of auxiliary qubits can enhance performance, yet there may exist an optimal threshold for a specific problem scale. We can select appropriate auxiliary qubits to enhance performance for tasks of different complexity.

Furthermore, we delve into the individual components that shape VQGLA's design, as shown in Table 6. *Repeated encoding* refers to encoding features at every block. *Synchronous encoding and learning* refers to adding features and learnable parameters as new learnable parameters. *Double interaction* refers to using a constraint and a variable layer in the graph message interaction layer. All configurations employ the same number of parameters. Results indicate that these three components are useful for the design of VQGLA.

Table 6: Ablation study *w.r.t* our components.

Repeated Encoding	**Syn. Encoding Learning**	**Double Interaction**	**Train**	**Test**
✗	✗	✗	0.0924	0.0953
✗	✗	✓	0.0876	0.0898
✓	✗	✓	0.0708	0.0726
✓	✗	✗	0.0738	0.0765
✓	✓	✗	0.0623	0.0659
✓	✓	✓	0.0557	0.0574

In addition, we studied the parameter transferability and the impact of noise on the model's performance. We train on the 20-qubit GNN-intractable MILPs and transfer their parameters into problems with 30, 40, and 50 qubits to test. n qubit represents a MILP graph dataset containing 200 different graphs with n nodes. Specifically, we use Qiskit's (Javadi-Abhari et al., 2024) matrix product state simulator, as well as IBM's noise model FakeWashingtonV2, with the backends built to mimic the behaviors of IBM Quantum systems. As shown in Table 7, the model parameters trained on the 20-qubit remain effective for the 50-qubit data, benefiting from VQGLA's parameter-sharing mechanism. This means that the parameters trained on small qubit datasets can provide a good initialization for larger qubit datasets, speeding up the training process. Moreover, while noise does have an impact on performance, the effect is within an acceptable range.

5.4 Comparison with Higher Order GNNs

To verify the expressiveness of our methods, we conducted an experiment on the recent dataset BREC (Wang & Zhang, 2024) used to evaluate GNN expressiveness, compared higher order

Table 7: Parameter transferability across qubits under noiseless and noisy conditions.

Qubit	20 (base)	30	40	50
Noiseless	1.0	0.967	0.908	0.862
Nosiy	0.995	0.928	0.864	0.825

Table 8: Performance comparison of GNNs on BREC datasets.

	Graphormer	δ-k-LGNN	NGNN	GSN	Ours
Basic	0.267	1.0	0.983	1.0	**1.0**
Regular	0.086	0.357	0.343	0.707	**0.964**
Extension	0.41	1.0	0.59	0.95	**1.0**

GNNs, including Transformer-based model Graphormer (Ying et al., 2021), k-WL hierarchy-based model δ-k-LGNN (Morris et al., 2020), subgraph-based model NGNN (Zhang & Li, 2021), and substructure-based model GSN (Bouritsas et al., 2022). The *Basic* dataset in BREC consists of 1-WL-indistinguishable graphs generated through exhaustive search and is designed to be non-regular. The *Regular* dataset contains regular graphs, further divided into simple regular graphs and strongly regular graphs, where 1-WL and 3-WL test fail, respectively. Including 4-vertex condition graphs and distance-regular graphs further increases the dataset's complexity. The *Extension* graphs bridge the gap between 1-WL and 3-WL, offering a more granular comparison for evaluating models beyond 1-WL. We employ Reliable Paired Comparison (RPC) (Wang & Zhang, 2024) to verify whether GNNs genuinely produce distinct outputs for a pair of graphs. As shown in Table 8, the results show that the proposed VQGLA not only achieves good performance on the Basic and Extension datasets but also outperforms other classical methods on the challenging Regular dataset.

6 The complexity and scalability of VQGLA

For a graph with N nodes and E edges, the node feature encoding layer involves $O(N)$ single-qubit gates, while the graph message interaction layer introduces $O(E)$ two-qubit gates. For a circuit with T blocks, the total number of gates scales as $O(T(N+E))$. For a graph with N nodes, our VQGLA typically requires $O(N)$ qubits. However, in the current NISQ era, both real quantum devices and classical simulators have a limited number of qubits. Therefore, inspired by how classical GNN algorithms handle large graph computations with limited resources, we have presented S-VQGLA to process large graphs with limited qubits. Specifically, we first employ the graph sampling technique GraphSAINT (Zeng et al.) to extract appropriately connected subgraphs, then apply our VQGLA model to these sample subgraphs and combine the obtained information of these subgraphs together so that the training process overall learns information of the full graph. In this way, for a graph with N nodes, we can sample m subgraphs for training, with each subgraph using at most k qubits.

Table 9: Performance comparison of graph classification accuracy on PROTEINS dataset.

Methods	GraphSAGE (Hamilton et al., 2017)	GIN (Xu et al., 2018)	GAT-GC (Zhang & Xie, 2020)	U2GNN (Nguyen et al., 2022a)	UGT (Lee et al., 2024)	S-VQGLA (**Ours**)
Accuracy (%)	73.0	76.2	76.8	78.5	80.1	**80.4**

Table 9 shows the performance of VQGLA on a commonly used graph classification dataset, PROTEINS, which consists of 1,113 graphs, and each graph has between 4 to 620 nodes. We extract appropriately connected subgraphs with at most 14 nodes, which can be processed using our 14-qubit VQGLA with 6 blocks. All subgraphs are input as a batch into the VQGLA, and we combine their results to predict the classification of the full graph. As we have observed, S-VQGLA not only outperforms message-passing based GNN methods (Hamilton et al., 2017; Xu et al., 2018; Zhang & Xie, 2020), but also slightly exceeds the recently proposed Graph Transformer-based methods (Nguyen et al., 2022a; Lee et al., 2024).

7 Conclusion

This paper introduces an expressive quantum graph learning framework aimed at addressing complex graph structural data, such as learning the MILP graph representation. Our proposed framework, VQGLA, uses the synchronous encoding and learning module to handle node and edge features, and presents a parameter-sharing mechanism and a carefully designed graph information interaction layer. We theoretically prove that VQGLA possesses permutation equivariance and invariance for nodes and edges. Moreover, the proposed graph information interaction layer leverages quantum entanglement to model the edges, enabling the capture of graph patterns that are challenging for classical methods. Numerical experiments demonstrate that our approach can overcome the fundamental limitations of traditional GNNs, achieving superior performance on MILP tasks that include GNN-intractable graphs. VQGLA also offers flexibility in configuration for general graphs, and the results of the BREC dataset highlight the versatility and separating power of VQGLA.

REFERENCES

Xing Ai, Zhihong Zhang, Luzhe Sun, Junchi Yan, and Edwin Hancock. Towards quantum graph neural networks:an ego-graph learning approach. *arXiv preprint arXiv:2201.05158*, 2022.

Hooman Askari-Nasab, Y Pourrahimian, E Ben-Awuah, and S Kalantari. Mixed integer linear programming formulations for open pit production scheduling. *Journal of Mining Science*, 47: 338–359, 2011.

Jacob Biamonte, Peter Wittek, Nicola Pancotti, Patrick Rebentrost, Nathan Wiebe, and Seth Lloyd. Quantum machine learning. *Nature*, 549(7671):195–202, 2017.

Giorgos Bouritsas, Fabrizio Frasca, Stefanos Zafeiriou, and Michael M Bronstein. Improving graph neural network expressivity via subgraph isomorphism counting. *IEEE Transactions on Pattern Analysis and Machine Intelligence*, 45(1):657–668, 2022.

Shaked Brody, Uri Alon, and Eran Yahav. How attentive are graph attention networks? In *Proceedings of the International Conference on Learning Representations*, 2022.

Ziang Chen, Jialin Liu, Xinshang Wang, and Wotao Yin. On representing mixed-integer linear programs by graph neural networks. In *Proceedings of the International Conference on Learning Representations*, 2023.

Christodoulos A. Floudas and Xiaoxia Lin. Mixed integer linear programming in process scheduling: Modeling, algorithms, and applications. *Annals of Operations Research*, 139(1):131–162, Oct 2005a. ISSN 1572-9338.

Christodoulos A Floudas and Xiaoxia Lin. Mixed integer linear programming in process scheduling: Modeling, algorithms, and applications. *Annals of Operations Research*, 139:131–162, 2005b.

Bernard Fortz and Michael Poss. An improved benders decomposition applied to a multi-layer network design problem. *Operations research letters*, 37(5):359–364, 2009.

Maxime Gasse, Didier Chételat, Nicola Ferroni, Laurent Charlin, and Andrea Lodi. Exact combinatorial optimization with graph convolutional neural networks. *Proceedings of the Advances in Neural Information Processing Systems*, 32, 2019.

Xueshi Guo, Casper R Breum, Johannes Borregaard, Shuro Izumi, Mikkel V Larsen, Tobias Gehring, Matthias Christandl, Jonas S Neergaard-Nielsen, and Ulrik L Andersen. Distributed quantum sensing in a continuous-variable entangled network. *Nature Physics*, 16(3):281–284, 2020.

Prateek Gupta, Elias B Khalil, Didier Chetélat, Maxime Gasse, Yoshua Bengio, Andrea Lodi, and M Pawan Kumar. Lookback for learning to branch. *arXiv preprint arXiv:2206.14987*, 2022.

Will Hamilton, Zhitao Ying, and Jure Leskovec. Inductive representation learning on large graphs. *Advances in neural information processing systems*, 30, 2017.

Ali Javadi-Abhari, Matthew Treinish, Kevin Krsulich, Christopher J Wood, Jake Lishman, Julien Gacon, Simon Martiel, Paul D Nation, Lev S Bishop, Andrew W Cross, et al. Quantum computing with qiskit. *arXiv preprint arXiv:2405.08810*, 2024.

Abhinav Kandala, Antonio Mezzacapo, Kristan Temme, Maika Takita, Markus Brink, Jerry M. Chow, and Jay M. Gambetta. Hardware-efficient variational quantum eigensolver for small molecules and quantum magnets. *Nature*, 549(7671):242–246, sep 2017.

Elias B Khalil, Christopher Morris, and Andrea Lodi. Mip-gnn: A data-driven framework for guiding combinatorial solvers. In *Proceedings of the AAAI Conference on Artificial Intelligence*, pp. 10219–10227, 2022.

Diederik P Kingma and Jimmy Ba. Adam: A method for stochastic optimization. *arXiv preprint arXiv:1412.6980*, 2014.

Martin Larocca, Frédéric Sauvage, Faris M Sbahi, Guillaume Verdon, Patrick J Coles, and Marco Cerezo. Group-invariant quantum machine learning. *PRX Quantum*, 3(3):030341, 2022.

O-Joun Lee et al. Transitivity-preserving graph representation learning for bridging local connectivity and role-based similarity. In *Proceedings of the AAAI Conference on Artificial Intelligence*, volume 38, pp. 12456–12465, 2024.

Jarrod R McClean, Sergio Boixo, Vadim N Smelyanskiy, Ryan Babbush, and Hartmut Neven. Barren plateaus in quantum neural network training landscapes. *Nature communications*, 9(1):4812, 2018.

Péter Mernyei, Konstantinos Meichanetzidis, and Ismail Ilkan Ceylan. Equivariant quantum graph circuits. In *Proceedings of the International Conference on Machine Learning*, pp. 15401–15420. PMLR, 2022.

Christopher Morris, Gaurav Rattan, and Petra Mutzel. Weisfeiler and leman go sparse: Towards scalable higher-order graph embeddings. *Advances in Neural Information Processing Systems*, 33: 21824–21840, 2020.

Dai Quoc Nguyen, Tu Dinh Nguyen, and Dinh Phung. Universal graph transformer self-attention networks. In *Companion Proceedings of the Web Conference 2022*, pp. 193–196, 2022a.

Quynh T Nguyen, Louis Schatzki, Paolo Braccia, Michael Ragone, Patrick J Coles, Frederic Sauvage, Martin Larocca, and M Cerezo. Theory for equivariant quantum neural networks. *arXiv preprint arXiv:2210.08566*, 2022b.

Joaquín Ossorio-Castillo and F Pena-Brage. Optimization of a refinery scheduling process with column generation and a quantum annealer. *Optimization and Engineering*, 23(3):1471–1488, 2022.

Alberto Peruzzo, Jarrod McClean, Peter Shadbolt, Man-Hong Yung, Xiao-Qi Zhou, Peter J Love, Alán Aspuru-Guzik, and Jeremy L O'brien. A variational eigenvalue solver on a photonic quantum processor. *Nature communications*, 5(1):4213, 2014.

Michael Ragone, Paolo Braccia, Quynh T Nguyen, Louis Schatzki, Patrick J Coles, Frederic Sauvage, Martin Larocca, and M Cerezo. Representation theory for geometric quantum machine learning. *arXiv preprint arXiv:2210.07980*, 2022.

A. Richards and J.P. How. Aircraft trajectory planning with collision avoidance using mixed integer linear programming. In *Proceedings of the American Control Conference*, volume 3, pp. 1936–1941 vol.3, 2002.

Louis Schatzki, Martin Larocca, Frederic Sauvage, and Marco Cerezo. Theoretical guarantees for permutation-equivariant quantum neural networks. *arXiv preprint arXiv:2210.09974*, 2022.

Tom Schouwenaars, Bart De Moor, Eric Feron, and Jonathan How. Mixed integer programming for multi-vehicle path planning. In *2001 European control conference (ECC)*, pp. 2603–2608. IEEE, 2001.

Yunsheng Shi, Zhengjie Huang, Shikun Feng, Hui Zhong, Wenjin Wang, and Yu Sun. Masked label prediction: Unified message passing model for semi-supervised classification. In *Proceedings of the International Joint Conference on Artificial Intelligence*, 2021.

Kristan Temme, Sergey Bravyi, and Jay M Gambetta. Error mitigation for short-depth quantum circuits. *Physical review letters*, 119(18):180509, 2017.

Ewout Van Den Berg, Zlatko K Minev, and Kristan Temme. Model-free readout-error mitigation for quantum expectation values. *Physical Review A*, 105(3):032620, 2022.

Petar Veličković, Guillem Cucurull, Arantxa Casanova, Adriana Romero, Pietro Liò, and Yoshua Bengio. Graph attention networks. In *Proceedings of the International Conference on Learning Representations*, 2018.

Guillaume Verdon, Trevor McCourt, Enxhell Luzhnica, Vikash Singh, Stefan Leichenauer, and Jack Hidary. Quantum graph neural networks. *arXiv preprint arXiv:1909.12264*, 2019.

Hanrui Wang, Yongshan Ding, Jiaqi Gu, Yujun Lin, David Z Pan, Frederic T Chong, and Song Han. Quantumnas: Noise-adaptive search for robust quantum circuits. In *High-Performance Computer Architecture*, pp. 692–708, 2022a.

Hao Wang, Yu Pan, and Wei Cui. Quantum-inspired solvers on mixed-integer linear programming problem. In *Proceedings of the Chinese Control Conference*, pp. 5693–5698. IEEE, 2022b.

Rui Wang, Zhiming Zhou, Tao Zhang, Ling Wang, Xin Xu, Xiangke Liao, and Kaiwen Li. Learning to branch in combinatorial optimization with graph pointer networks, 2023.

Yanbo Wang and Muhan Zhang. An empirical study of realized gnn expressiveness. In *Forty-first International Conference on Machine Learning*, 2024.

Boris Weisfeiler and Andrei Leman. The reduction of a graph to canonical form and the algebra which appears therein. *Nauchno-Technicheskaya Informatsia*, 2(9):12–16, 1968.

Yadong Wu, Juan Yao, Pengfei Zhang, and Hui Zhai. Expressivity of quantum neural networks. *Physical Review Research*, 3(3):L032049, 2021.

Keyulu Xu, Weihua Hu, Jure Leskovec, and Stefanie Jegelka. How powerful are graph neural networks? *Proceedings of the International Conference on Learning Representations*, 2018.

Xinyu Ye, Ge Yan, and Junchi Yan. Towards quantum machine learning for constrained combinatorial optimization: a quantum qap solver. In *Proceedings of the International Conference on Machine Learning)*, 2023.

Chengxuan Ying, Tianle Cai, Shengjie Luo, Shuxin Zheng, Guolin Ke, Di He, Yanming Shen, and Tie-Yan Liu. Do transformers really perform badly for graph representation? *Advances in neural information processing systems*, 34:28877–28888, 2021.

Hanqing Zeng, Hongkuan Zhou, Ajitesh Srivastava, Rajgopal Kannan, and Viktor Prasanna. Graph-saint: Graph sampling based inductive learning method. In *International Conference on Learning Representations*.

Muhan Zhang and Pan Li. Nested graph neural networks. *Advances in Neural Information Processing Systems*, 34:15734–15747, 2021.

Shuo Zhang and Lei Xie. Improving attention mechanism in graph neural networks via cardinality preservation. In *IJCAI: proceedings of the conference*, volume 2020, pp. 1395. NIH Public Access, 2020.

Zhongqi Zhao, Lei Fan, and Zhu Han. Hybrid quantum benders' decomposition for mixed-integer linear programming. In *IEEE Wireless Communications and Networking Conference (WCNC)*, pp. 2536–2540. IEEE, 2022.

Jin Zheng, Qing Gao, and Yanxuan Lü. Quantum graph convolutional neural networks. In *Proceedings of the Chinese Control Conference*, pp. 6335–6340. IEEE, 2021.

A Related Work

Quantum Graph Neural Networks Various quantum graph neural networks have been presented. (Verdon et al., 2019) proposed a class of graph neural networks by defining operations in terms of Hamiltonians based on the graph structure. However, their models are restricted to Hamiltonians of specific forms, thereby cannot flexibly and efficiently encode classical high-dimensional node or edge features of the graphs to solve some classical tasks. (Zheng et al., 2021) designed a specific quantum graph convolutional neural network (QGCN), which uses an amplitude encoding method to encode node and edge features and employs qubits representing edges as control qubits to apply unitaries to the two qubits representing nodes connected by that edge. Nevertheless, the usage of edge qubits will lead to the number of qubits of the model scales quadratically with the number of nodes. Moreover, the pooling layer and measurement operator of QGCN will indeed result in the loss of permutation invariance of the entire model. (Ai et al., 2022) presented an ego-graph based Quantum Graph Neural Network (egoQGNN), which decomposes the input graph into smaller-scale subgraphs and feeds them into the circuit. However, due to the use of entanglement layers within the model, it still does not possess permutation invariance.

Equivariant Quantum Neural Networks Recently, a nascent field named geometric quantum machine learning (GQML) (Larocca et al., 2022; Nguyen et al., 2022b) has been developed, which leverages the machinery of group and representation theory (Ragone et al., 2022) to build quantum architectures that encode symmetry information about the problem. Schatzki et al. (2022) provide an analytical study of S_n-equivariant QNNs and prove that they do not suffer from barren plateaus, quickly reach overparametrization, and can generalize well from small amounts of data. The equivariant QNNs can used to learn various problems with permutation symmetries abound, such as molecular systems, condensed matter systems, and distributed quantum sensors (Peruzzo et al., 2014; Guo et al., 2020), namely, they are also not specifically designed to solve classical graph tasks. (Mernyei et al., 2022) first proposed a theoretical recipe for building permutation equivariant quantum graph circuits (EQGC) and aggregated the output of the quantum circuit by classical functions to ensure permutation invariance of the model. Nevertheless, the EQGC does not provide the specific circuit implementation and does not consider the case of weighted graphs in their model. In addition, another QNN with permutation equivariance (Ye et al., 2023) is proposed, which is specially designed for solving quadratic assignment problems, but their model only encodes the graph information and then employs the shared problem-agnostic ansatz to learn the representation of each node. Thus, their model does not contain the learnable graph message interaction layer.

Quantum Algorithms for MILP Mixed-Integer Linear Programming (MILP) is a mathematical optimization approach that aims to find the best solution to a linear objective function while imposing constraints on some or all of the variables to be integers. MILP is widely used in various practical applications such as process scheduling (Floudas & Lin, 2005a), transportation (Richards & How, 2002), and network design (Fortz & Poss, 2009). Recently, researchers have endeavored to employ quantum computing to assist in solving the MILP. (Zhao et al., 2022) proposed a hybrid quantum-classical Benders' decomposition algorithm, which decomposes an MILP problem into a Quadratic unconstrained binary optimization (QUBO) problem solved by quantum computer and a subproblem easily tackled by classical computers. (Ossorio-Castillo & Pena-Brage, 2022) described an algorithm based on Dantzig–Wolfe decomposition. Different from (Zhao et al., 2022), the algorithm then solves several either continuous or binary subproblems instead of a mixed one. (Wang et al., 2022b) pointed out that quantum-inspired Ising machines can be used to solve MILPs by reducing them into Ising models. However, the above algorithms are based on unconstrained Ising models, while MILPs are subject to complex constraints. Their common solution is to introduce a penalty to the algorithm. A proper penalty is of great importance because an extremely large penalty may cause the quantum annealer to malfunction since it will explode the coefficients, while a soft penalty may make the quantum annealer ignore the corresponding constraints (Zhao et al., 2022). However, there is no instruction on how to tune the penalty, and it may even be different for various MILP problems. In contrast, our approach leverages QML to represent MILP problems, thereby pioneering a novel direction for harnessing quantum computing in aiding MILP solutions, there is promising for witnessing the emergence of new paradigms that combine quantum and classical methods for MILP solving.

B The Basics of Quantum Computing

Single-qubit Quantum State. In quantum computing, the fundamental building blocks of computation are qubits (short for quantum bits), which are the quantum analog of classical bits. Unlike

classical bits, which can only take on one of two possible values (0 or 1), a qubit can exist in a superposition of the two states, represented by the vector:

$$|\psi\rangle = \alpha_1|0\rangle + \alpha_2|1\rangle, \tag{5}$$

where $|0\rangle$ and $|1\rangle$represent the two basis states of one qubit, and α_1 and α_2 are complex numbers that satisfy the normalization condition $|\alpha_1|^2 + |\alpha_2|^2 = 1$. When $|\psi\rangle$ is measured, it will collapse to either the $|0\rangle$ or $|1\rangle$ state with a probability $|\alpha_1|^2$ or $|\alpha_2|^2$.

Mathematically, the quantum state of one qubit can be denoted as a complex 2-dimensional vector, e.g., $|0\rangle = [1, 0]^T$, $|1\rangle = [0, 1]^T$, and $|\psi\rangle = [\alpha_1, \alpha_2]^T$. The Bloch sphere is a sphere of radius 1, which is a useful tool for visualizing the state of a single qubit. Any other state of one qubit can be represented by a point on the surface of the sphere, and you can see them through this online tool [2].

Multi-qubit Quantum State. Multi-qubit quantum states are an extension of single-qubit quantum states, and a N-qubit quantum state can be represented as a complex 2^N-dimensional vector in Hilbert space. This is why quantum systems are often described as living in a 2^N-dimensional Hilbert space. More specifically, a two-qubit system can be represented as $|\phi\rangle = \alpha_1|00\rangle + \alpha_2|01\rangle + \alpha_3|10\rangle + \alpha_4|11\rangle$, where $\sum_{i=1}^{2^2} |\alpha_i^2| = 1$ and $|00\rangle$ represent the tensor product $|0\rangle \otimes |0\rangle$.

Quantum Circuits. Quantum circuits are constructed using quantum gates, which are analogous to classical logic gates. Some commonly used single-qubit gates include the Pauli-X gate, the Pauli-Y gate, and the Pauli-Z gate. They can be represented by the unitary matrix:

$$\sigma_x = \begin{pmatrix} 0 & 1 \\ 1 & 0 \end{pmatrix}, \sigma_y = \begin{pmatrix} 0 & -i \\ i & 0 \end{pmatrix}, \sigma_z = \begin{pmatrix} 1 & 0 \\ 0 & -1 \end{pmatrix}. \tag{6}$$

The Controlled-NOT (CNOT) gate is a two-qubit gate that flips the second qubit (target) if the first qubit (control) is in the $|1\rangle$ state. We provide the matrix forms of common quantum gates in Table 10. When a quantum gate acts on a quantum state $|\psi\rangle$, it transforms this state to another quantum state $|\psi'\rangle$, according to the mathematical operation $|\psi'\rangle = U|\psi\rangle$, where U represents the unitary matrix associated with the quantum gate.

Parameterized Quantum Circuits. Parameterized quantum circuits (PQCs) consist of parameterized gates and offer a concrete way to implement quantum machine learning algorithms. Specifically, the common parameterized quantum gates are listed in Table 10. The parameters (e.g., θ) in the quantum gate can be either learnable parameters for optimizers or classical information that we want to encode.

Quantum Machine Learning. A quantum machine learning model can be constructed using a sequence of parameterized quantum gates. The initial quantum states can be transformed into the output quantum states. By measuring the output of the quantum circuit, we can convert quantum information into classical information, which can be used to calculate the cost function of the optimization task. We can use classical optimizers to minimize the cost function by adjusting the parameters of quantum gates.

C FORMULAS OF EACH LAYER IN VQGLA

In VQGLA, the single-qubit gate can be written as the unitary matrix from. For example, $K(\theta) = \exp(-\mathbf{i}\frac{\theta}{2}P^K)$, where $P^K \in \{\sigma_x, \sigma_y, \sigma_z\}$. Similarly, $W(\theta) = \exp(-\mathbf{i}\frac{\theta}{2}P^W)$, $D(\theta) = \exp(-\mathbf{i}\frac{\theta}{2}P^D)$, $G(\theta) = \exp(-\mathbf{i}\frac{\theta}{2}P^G)$.

Based on this, the unitary matrix of the node feature layer of Fig. 4 contains:

$$\begin{aligned} U_W(c, u, b, \alpha_t) &= \exp(-\mathbf{i}(\textstyle\sum_{i=1}^{q}((c_i+\alpha_{t,1})P_{2i}^W \ + (u_i+\alpha_{t,2})P_{2i+1}^W) + \sum_{j=1}^{p}(b_j+\alpha_{t,5})P_{2q+j}^W)), \\ U_D(l, \epsilon, \circ, \alpha_t) &= \exp(-\mathbf{i}(\textstyle\sum_{i=1}^{q}((l_i+\alpha_{t,3})P_{2i}^D \ + (\epsilon_i+\alpha_{t,4})P_{2i+1}^D) + \sum_{j=1}^{p}(\circ_j+\alpha_{t,6})P_{2q+j}^D)), \\ \text{where } P_{2i}^W &= \underbrace{I \otimes \cdots \otimes}_{2i-1} P^W \underbrace{\otimes \cdots \otimes I}_{q+p-2i}. \end{aligned} \tag{7}$$

[2] https://javafxpert.github.io/grok-bloch/

Table 10: Common quantum gates.

Operator	**Gate(s)**	**Matrix**
Pauli-X (X, σ_x)	X	$\begin{bmatrix} 0 & 1 \\ 1 & 0 \end{bmatrix}$
Pauli-Y (Y, σ_y)	Y	$\begin{bmatrix} 0 & -i \\ i & 0 \end{bmatrix}$
Pauli-Z (Z, σ_z)	Z	$\begin{bmatrix} 1 & 0 \\ 0 & -1 \end{bmatrix}$
Rotation-Z ($R_Z(\theta)$)	RZ	$\begin{bmatrix} e^{-\mathrm{i}\frac{\theta}{2}} & 0 \\ 0 & e^{\mathrm{i}\frac{\theta}{2}} \end{bmatrix}$
Rotation-Y ($R_Y(\theta)$)	RY	$\begin{bmatrix} \cos(\frac{\theta}{2}) & -\sin(\frac{\theta}{2}) \\ \sin(\frac{\theta}{2}) & \cos(\frac{\theta}{2}) \end{bmatrix}$
Rotation-X ($R_X(\theta)$)	RX	$\begin{bmatrix} \cos(\frac{\theta}{2}) & -\mathrm{i}\sin(\frac{\theta}{2}) \\ -\mathrm{i}\sin(\frac{\theta}{2}) & \cos(\frac{\theta}{2}) \end{bmatrix}$
Controlled Not (CNOT, CX)	$\bullet\!-\!\oplus$	$\begin{bmatrix} 1 & 0 & 0 & 0 \\ 0 & 1 & 0 & 0 \\ 0 & 0 & 0 & 1 \\ 0 & 0 & 1 & 0 \end{bmatrix}$
Controlled RZ ($C_{RZ}(\theta)$)	$\bullet\!-\!RZ$	$\begin{bmatrix} 1 & 0 & 0 & 0 \\ 0 & 1 & 0 & 0 \\ 0 & 0 & e^{-\mathrm{i}\frac{\theta}{2}} & 0 \\ 0 & 0 & 0 & e^{\mathrm{i}\frac{\theta}{2}} \end{bmatrix}$
Controlled RY ($C_{RY}(\theta)$)	$\bullet\!-\!RY$	$\begin{bmatrix} 1 & 0 & 0 & 0 \\ 0 & 1 & 0 & 0 \\ 0 & 0 & \cos(\frac{\theta}{2}) & -\sin(\frac{\theta}{2}) \\ 0 & 0 & \sin(\frac{\theta}{2}) & \cos(\frac{\theta}{2}) \end{bmatrix}$
Controlled RX ($C_{RX}(\theta)$)	$\bullet\!-\!RX$	$\begin{bmatrix} 1 & 0 & 0 & 0 \\ 0 & 1 & 0 & 0 \\ 0 & 0 & \cos(\frac{\theta}{2}) & -\mathrm{i}\sin(\frac{\theta}{2}) \\ 0 & 0 & -\mathrm{i}\sin(\frac{\theta}{2}) & \cos(\frac{\theta}{2}) \end{bmatrix}$

The graph message interaction layer of Fig. 5 contains:

$$
\begin{aligned}
&U_K^V(A, \beta_{t,1}) = \exp(-\mathbf{i}(\sum_{(i,j)\in\mathcal{E}} (A_{i,j} + \beta_{t,1})(I - \sigma_z)_{2i} P_{2q+j}^K)),\\
&U_K^{V'}(A, \beta_{t,2}) = \exp(-\mathbf{i}(\sum_{(i,j)\in\mathcal{E}} (A_{i,j} + \beta_{t,2})(I - \sigma_z)_{2i+1} P_{2q+j}^K)),\\
&U_G^V(\beta_{t,3}) = \exp(-\mathbf{i}(\sum_i \beta_{t,3}(I - \sigma_z)_{2i+1} P_{2i}^G)),\\
&U_K^S(A, \beta_{t,4}) = \exp(-\mathbf{i}(\sum_{(i,j)\in\mathcal{E}} (A_{i,j} + \beta_{t,4})(I - \sigma_z)_{2q+j} P_{2i}^K)),\\
&U_K^{S'}(A, \beta_{t,5}) = \exp(-\mathbf{i}(\sum_{(i,j)\in\mathcal{E}} (A_{i,j} + \beta_{t,5})(I - \sigma_z)_{2q+j} P_{2i+1}^K)),\\
&U_G^S(\beta_{t,6}) = \exp(-\mathbf{i}(\sum_j \beta_{t,6} P_{2q+j}^G)).
\end{aligned}
\tag{8}
$$

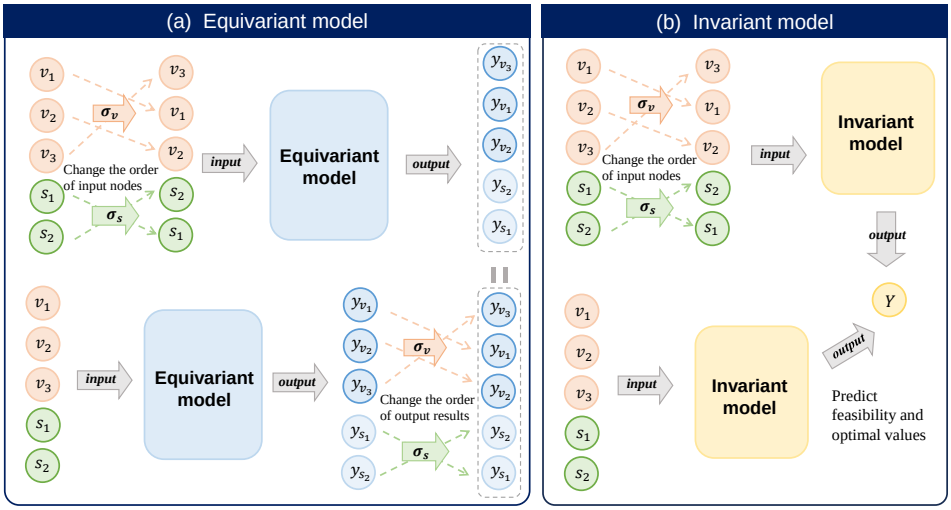

Figure 7: Diagram of the properties of equivariant (a) and invariant (b) models. For equivariant models, when the input node has a permutation σ, the output is equivalent to the original one with the same permutation σ. For invariant models, the permutation of input nodes will not affect output Y.

D THEOREMS AND PROOFS OF THE EQUIVARIANCE

D.1 THE DETAILS OF DEFINITION 1

$\Lambda_q \in \mathbb{B}^{q\times q}$ and $\Lambda_p \in \mathbb{B}^{p\times p}$ are permutation matrices representing a permutation $\pi_q \in \mathcal{S}^q$ and $\pi_p \in \mathcal{S}^p$, respectively. $\mathcal{S}^q$ and $\mathcal{S}^p$ are the groups containing all permutations on the q variable nodes and p constraint nodes, respectively. After the MILP graph undergoes permutation π_q and π_p, the feature set of the variable nodes and the feature set of the constraint nodes become $\Lambda_q \mathrm{H}^{\mathrm{V}}$ and $\Lambda_p \mathrm{H}^{\mathrm{S}}$, respectively. Then, the adjacency matrix between variable nodes and constraint nodes of the MILP graph $A \in \mathbb{R}^{p\times q}$ is transformed to $\Lambda_p A \Lambda_q$. We define a permutation π_{q+p} on the $(q+p)$ elements to indicate the overall permutation on all nodes of the MILP graph. π_{q+p} consists of two distinct parts: the first q elements follow the permutation π_q, and the subsequent p elements follow π_p. $\widetilde{\Lambda}$ is the unitary representation of π_{q+p}, which indicates the permutation of qubits representing nodes. $\widetilde{\Lambda}$ can be implemented by applying a series of $SWAP$ gates to the quantum circuit. The detailed proof and formulation are as follows.

It is known that any permutation can be expressed as a product of transpositions. The transposition refers to a simple permutation that just swaps two elements. Suppose that the permutation π_{q+p} contains z transpositions, i.e., $\pi_{q+p} = (\delta_{11}, \delta_{12})...(\delta_{i1}, \delta_{i2})...(\delta_{z1}, \delta_{z2})$. Given that a n-qubit quantum circuit and suppose that one qubit represents one node, *i.e.*, $n = p + q$, a transposition $(\delta_{z1}, \delta_{z2})$ can be represented by a $SWAP_{(\delta_{z1},\delta_{z2})}$ gate to exchange the δ_{z1}-th qubit and δ_{z2}-th qubit of the quantum circuit. Hence, the corresponding unitary $\widetilde{\Lambda} = \widetilde{\Lambda}_{\delta_1}\widetilde{\Lambda}_{\delta_2}...\widetilde{\Lambda}_{\delta_i}...\widetilde{\Lambda}_{\delta_z}$ is equal to

$$SWAP_{(\delta_{11},\delta_{12})}...SWAP_{(\delta_{i1},\delta_{i2})}...SWAP_{(\delta_{z1},\delta_{z2})}. \tag{9}$$

That is, we decompose a complex permutation into a series of transposition, so that we can get:

Defintion D.1. *If the quantum circuit U is equivariant for any transpositions $(\delta_{i1}, \delta_{i2})$, i.e.,*

$$U(\Lambda_{p\delta_i} A \Lambda_{q\delta_i}, \Lambda_{q\delta_i} H^V, \Lambda_{p\delta_i} H^S, \Theta) = \widetilde{\Lambda}^{\dagger}_{\delta_i} \cdot U(A, H^V, H^S, \Theta) \cdot \widetilde{\Lambda}_{\delta_i},$$

the circuit is equivariant for the permutation π_{q+p}, where $\Lambda_{p\delta_i}$ and $\Lambda_{q\delta_i}$ are the permutation matrices corresponding to the permutation $(\delta_{i1}, \delta_{i2})$.

Based on Definition D.1, we can derive Definition 1 by using Eq. 9.

$$
\begin{aligned}
&\widetilde{\Lambda}^{\dagger} \cdot U(A, \mathrm{H}^{\mathrm{V}}, \mathrm{H}^{\mathrm{S}}, \Theta) \cdot \widetilde{\Lambda} \\
&= SWAP_{(\delta_{z1},\delta_{z2})}...SWAP_{(\delta_{11},\delta_{12})} \cdot U(A, \mathrm{H}^{\mathrm{V}}, \mathrm{H}^{\mathrm{S}}, \Theta) \cdot SWAP_{(\delta_{11},\delta_{12})}...SWAP_{(\delta_{z1},\delta_{z2})}, \\
&= SWAP_{(\delta_{z1},\delta_{z2})}...SWAP_{(\delta_{21},\delta_{22})} U(\Lambda_{p\delta_1} A \Lambda_{q\delta_1}, \Lambda_{q\delta_1}\mathrm{H}^{\mathrm{V}}, \Lambda_{p\delta_1}\mathrm{H}^{\mathrm{S}}, \Theta) SWAP_{(\delta_{21},\delta_{22})}...SWAP_{(\delta_{z1},\delta_{z2})} \\
&= U(\Lambda_{p\delta_1...\delta_z} A \Lambda_{q\delta_1...\delta_z}, \Lambda_{q\delta_1...\delta_z}\mathrm{H}^{\mathrm{V}}, \Lambda_{p\delta_1...\delta_z}\mathrm{H}^{\mathrm{S}}, \Theta) \\
&= U(\Lambda_p A \Lambda_q, \Lambda_q \mathrm{H}^{\mathrm{V}}, \Lambda_p \mathrm{H}^{\mathrm{S}}, \Theta)
\end{aligned}
\tag{10}
$$

By the associative law of matrix multiplication, we can combine the middle three terms of the formula until the last transpositions. In the final, $\Lambda_{p\delta_1...\delta_z} = \Lambda_p$ and $\Lambda_{q\delta_1...\delta_z} = \Lambda_q$ reprsent the permutation matrices corresponding to the permutation $\pi_{q+p} = (\delta_{11}, \delta_{12})...(\delta_{i1}, \delta_{i2})...(\delta_{z1}, \delta_{z2})$. Thereby, we can obtain Definition 1.

D.2 The Details of Theorem 1

We can decompose Theorem 1 into the following theorems and corollary for clearer proof.

Theorem D.1. ***(U_{qgl} is Equivariant).*** *The circuit $U_{qgl}(A, H^V, H^S, \Theta)$ of the proposed VQGLA is a permutation equivariant circuit.*

Theorem D.2. ***($\Phi(A, H, \Theta)$ is an Equivariant Mapping).*** *After Pauli-Z measurement, the output of the VQGLA is permutation equivariant.*

Corollary D.1. ***($\phi(A, H)_{fea}$ is an Invariant Mapping).*** *The mapping of VQGLA to predict the feasibility of instance $\phi(A, H)_{fea}$ is permutation invariant.*

D.2.1 The Proof of Theorem D.1

These two circuits in the quantum circuit are permutation-dependent and permutation-independent circuits. Permutation-dependent circuit refers to the quantum circuit composed of gates related to input node features or edge features. Permutation independent circuit is defined as:

Defintion D.2. ***(Permutation Independent Circuit).*** *A parameterized quantum circuit $U_{ind})$ is permutation independent for MILP graphs (A, H^V, H^S) if $U_{ind}(\Lambda_p A \Lambda_q, \Lambda_q H^V, \Lambda_p H^S, \Theta) = U_{ind}(\Theta)$, and*

$$\widetilde{\Lambda}^{\dagger} U_{ind}(\Theta) = U_{ind}(\Theta)\widetilde{\Lambda} = U_{ind}(\Theta). \tag{11}$$

We can derive the permutation equivariance of the circuit that only contain permutation equivariant circuit and permutation indepentent circuit.

Corollary D.2. ***(Equivariant $\times$ Independent = Equivariant).*** *If a quantum circuit $U = U_{eq}U_{ind}$, where U_{eq} represents the permutation equivariant circuit and U_{ind} represents the permutation independent circuit, then U is the permutation equivariant circuit.*

Proof. It is known that

$$
\begin{aligned}
U_{eq}(A, \mathrm{H}^{\mathrm{V}}, \mathrm{H}^{\mathrm{S}}) &= \widetilde{\Lambda} \cdot U_{eq}(\Lambda_p A \Lambda_q, \Lambda_q \mathrm{H}^{\mathrm{V}}, \Lambda_p \mathrm{H}^{\mathrm{S}}) \cdot \widetilde{\Lambda}^{\dagger}, \\
\widetilde{\Lambda}^{\dagger} U_{ind}(\Theta) &= U_{ind}(\Theta)\widetilde{\Lambda}^{\dagger} = U_{ind}(\Theta).
\end{aligned}
$$

Therefore, we can obtain

$$
\begin{aligned}
U(A, \mathrm{H}^{\mathrm{V}}, \mathrm{H}^{\mathrm{S}}, \Theta) &= U_{eq}(A, \mathrm{H}^{\mathrm{V}}, \mathrm{H}^{\mathrm{S}}) U_{indd}(\Theta) = \widetilde{\Lambda} \cdot U_{eq}(\Lambda_p A \Lambda_q, \Lambda_q \mathrm{H}^{\mathrm{V}}, \Lambda_p \mathrm{H}^{\mathrm{S}}) \cdot \widetilde{\Lambda}^{\dagger} \cdot U_{ind}(\Theta) \\
&= \widetilde{\Lambda} \cdot U_{eq}(\Lambda_p A \Lambda_q, \Lambda_q \mathrm{H}^{\mathrm{V}}, \Lambda_p \mathrm{H}^{\mathrm{S}}) \cdot \widetilde{\Lambda}^{\dagger} \cdot \widetilde{\Lambda} \cdot U_{ind}(\Theta) \cdot \widetilde{\Lambda}^{\dagger} \\
&= \widetilde{\Lambda} \cdot U_{eq}(\Lambda_p A \Lambda_q, \Lambda_q \mathrm{H}^{\mathrm{V}}, \Lambda_p \mathrm{H}^{\mathrm{S}}) \cdot U_{ind}(\Theta) \cdot \widetilde{\Lambda}^{\dagger} \\
&= \widetilde{\Lambda} \cdot U(\Lambda_p A \Lambda_q, \Lambda_q \mathrm{H}^{\mathrm{V}}, \Lambda_p \mathrm{H}^{\mathrm{S}}, \Theta) \cdot \widetilde{\Lambda}^{\dagger},
\end{aligned}
$$

which indicates the circuit satisfies the definition of permutation equivariance.

On the other hand, VQGLA contains many layers, and we can demonstrate the permutation equivariance of VQGLA by proving the permutation equivariance of each layer in VQGLA.

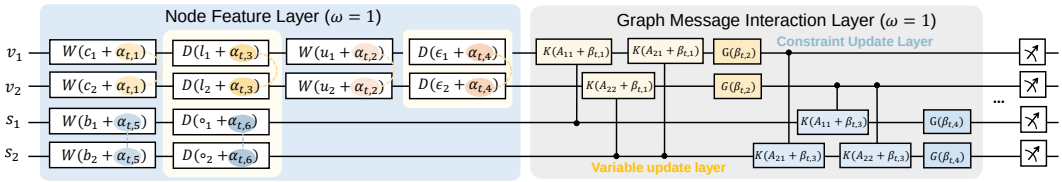

Figure 8: The framework of VQGLA with one qubit represents one node (*i.e.*, $\omega = 1$).

Theorem D.3. ***(Equivariance of Γ-layered circuit).*** *A Γ-layered quantum circuit $U(A, H^V, H^S, \Theta) = \prod_{t=1}^{\Gamma} U^t(A, H^V, H^S, \Theta_t)$ is permutation equivariant iff every layer U^t is permutation equivariant.*

Proof. U^t is permutation equivariant means that

$$U^t(A, \mathrm{H}^{\mathrm{V}}, \mathrm{H}^{\mathrm{S}}, \Theta_t) = \widetilde{\Lambda} \cdot U^t(\Lambda_p A \Lambda_q, \Lambda_q \mathrm{H}^{\mathrm{V}}, \Lambda_p \mathrm{H}^{\mathrm{S}}, \Theta_t) \cdot \widetilde{\Lambda}^{\dagger}.$$

Therefore,

$$U(A, \mathrm{H}^{\mathrm{V}}, \mathrm{H}^{\mathrm{S}}, \Theta) = \prod_{t=1}^{\Gamma} U^t(A, \mathrm{H}^{\mathrm{V}}, \mathrm{H}^{\mathrm{S}}, \Theta_t) = \prod_{t=1}^{\Gamma} \widetilde{\Lambda} \cdot U^{\top}(\Lambda_p A \Lambda_q, \Lambda_q \mathrm{H}^{\mathrm{V}}, \Lambda_p \mathrm{H}^{\mathrm{S}}, \Theta_t) \cdot \widetilde{\Lambda}^{\dagger},$$

where $\widetilde{\Lambda}$ and $\widetilde{\Lambda}^{\dagger}\widetilde{\Lambda} = I$. Hence,

$$U(A, \mathrm{H}^{\mathrm{V}}, \mathrm{H}^{\mathrm{S}}, \Theta) = \widetilde{\Lambda}(\prod_{t=1}^{\Gamma} U^{(}\Lambda_p A \Lambda_q, \Lambda_q \mathrm{H}^{\mathrm{V}}, \Lambda_p \mathrm{H}^{\mathrm{S}}, \Theta_t))\widetilde{\Lambda}^{\dagger} = \widetilde{\Lambda} U(\Lambda_p A \Lambda_q, \Lambda_q \mathrm{H}^{\mathrm{V}}, \Lambda_p \mathrm{H}^{\mathrm{S}}, \Theta)\widetilde{\Lambda}^{\dagger}.$$

Each layer of VQGLA has the same circuit structure and can be decomposed into $U_x(\mathrm{H}^{\mathrm{V}}, \mathrm{H}^{\mathrm{S}}, \alpha_t)U_g(A, \beta_t)U_a(\gamma_t)$. Moreover, $U_a(\gamma_t)$ is a permutation independent circuit. Therefore, by Corollary D.2 and Corollary D.1, we only need to prove that $U_x(\mathrm{H}^{\mathrm{V}}, \mathrm{H}^{\mathrm{S}}, \alpha_t)$ and $U_g(A, \beta_t)$ are permutation equivariant for any transpositions $(\delta_{i1}, \delta_{i2})$.

Equivariance of the Node Feature Layer

Take Fig. 8 as an example, *i.e.*, one qubit represents one node, $U_x(\mathrm{H}^{\mathrm{V}}, \mathrm{H}^{\mathrm{S}}, \alpha_t)$ can be written as $U_{v_1} \otimes U_{v_2} \otimes U_{s_1} \otimes U_{s_2}$, where $U_{v_i} = W(c_i + \alpha_{t,1})D(l_i + \alpha_{t,3})W(u_i + \alpha_{t,2})D(\epsilon_i + \alpha_{t,4}), i = \{1, ..., q\}$ and $U_{s_j} = W(b_j + \alpha_{t,5})D(\circ_j + \alpha_{t,6}), j = \{1, ..., p\}$. When the node permutation changes, $U_x(\Lambda_q \mathrm{H}^{\mathrm{V}}, \Lambda_p \mathrm{H}^{\mathrm{S}}, \alpha_t) = U_{v_{\pi_q(1)}} \otimes U_{v_{\pi_q(2)}} \otimes U_{s_{\pi_p(1)}} \otimes U_{s_{\pi_p(2)}}$. As we can see, the node permutation is transformed into the permutation of the order of tensor products of unitary matrices on individual qubits. Suppose there is a n-qubit arbitrary quantum state

$$|\psi\rangle = \sum C_{d_1 ... d_j ... d_n} |d_1 ... d_j ... d_n\rangle, d_j \in \{0, 1\},$$

where $C_{d_1 ... d_j ... d_n}$ is the amplitude of the basic state $|d_1 ... d_j ... d_n\rangle$. Take $|\psi\rangle$ as input to $U = U_1 \otimes ... U_j ... \otimes U_n$. For a transposition $(\delta_{i1}, \delta_{i2})$,

$$\begin{aligned}
&SWAP_{(\delta_{i1},\delta_{i2})}|\psi\rangle = \sum C_{d_1 ... d_{\delta_{i1}} ... d_{\delta_{i2}} ... d_n} |d_1 ... d_{\delta_{i2}} ... d_{\delta_{i1}} ... d_n\rangle, \\
&USWAP_{(\delta_{i1},\delta_{i2})}|\psi\rangle = \sum C_{d_1 ... d_{\delta_{i1}} ... d_{\delta_{i2}} ... d_n} U_1|d_1\rangle \otimes ... \otimes U_{\delta_{i1}}|d_{\delta_{i2}}\rangle \otimes ... U_{\delta_{i2}}|d_{\delta_{i1}}\rangle \otimes ... U_n|d_n\rangle, \\
&SWAP_{(\delta_{i1},\delta_{i2})}USWAP_{(\delta_{i1},\delta_{i2})}|\psi\rangle = \sum C_{d_1 ... d_{\delta_{i1}} ... d_{\delta_{i2}} ... d_n} U_1|d_1\rangle \otimes ... \otimes U_{\delta_{i2}}|d_{\delta_{i1}}\rangle \otimes ... U_{\delta_{i1}}|d_{\delta_{i2}}\rangle \otimes ... U_n|d_n\rangle \\
&= U_1 \otimes ... \otimes U_{\delta_{i2}} \otimes ... \otimes U_{\delta_{i1}} \otimes ... \otimes U_n|\psi\rangle.
\end{aligned} \tag{12}$$

Therefore, we can obtain $SWAP_{(\delta_{i1},\delta_{i2})}U_1 \otimes ... \otimes U_{\delta_{i1}} \otimes ... \otimes U_{\delta_{i2}} \otimes ... \otimes U_n SWAP_{(\delta_{i1},\delta_{i2})} = U_1 \otimes ... \otimes U_{\delta_{i2}} \otimes ... \otimes U_{\delta_{i1}} \otimes ... \otimes U_n$, which indicates the unitary U satisfies the definition of the equivariance.

Equivariance of the Graph Interaction Layer

As shown in Fig. 8, the variable update layer has a similar structure to the constraint update layer. Moreover, the layer that consists of $G(\beta_t)$ is the permutation independent circuit. Therefore, according to Corollary D.2, we only need to prove that the layer that consists of controlled-K gates is

permutation equivariant. It is known that $CK(\theta)_{2,1} = I \otimes |0\rangle\langle 0| + K(\theta) \otimes |1\rangle\langle 1|$, where the first qubit is the target qubit and the second qubit is the control qubit. Moreover,

$$SWAP_{(2,1)} CK(\theta)_{2,1} SWAP_{(2,1)} = |0\rangle\langle 0| \otimes I + |1\rangle\langle 1| \otimes K(\theta) = CK(\theta)_{1,2}. \tag{13}$$

For $n(= q + p)$-qubit circuit,

$$CK(A_{jk}+\beta_t)_{q+j,k} = I_1 \otimes ... \otimes |0\rangle\langle 0|_{q+j} \otimes ... \otimes I_n + I_1 \otimes K(A_{jk}+\beta_t)_k \otimes ... \otimes |1\rangle\langle 1|_{q+j} \otimes ... \otimes I_n,$$

where the index of the matrix represents the index of qubit that the matrix acted on. For brevity, we set $\theta_{jk} = A_{jk} + \beta_t$, $\mathbf{0} = |0\rangle\langle 0|$, $\mathbf{1} = |1\rangle\langle 1|$, and the edge set of the graph is $\mathcal{E}$. As we can see, the double-qubit quantum gate is only related to the permutation of the qubit $(q + j)$ or qubit k. Assume that there are two transpositions $(q + j, q + \delta^s(j))$ and $(k,)$ to exchange the place of the qubits, and $SWAP'$ denot Considering a n-qubit arbitrary quantum state

$$|\psi\rangle = \sum C_{d_1...d_i...d_n} |d_1...d_k...d_{\delta^v(k)}...d_{q+j}...d_{q+\delta^s(j)}...d_n\rangle, d_i \in \{0, 1\}.$$

$$\begin{aligned}
&SWAP'|\psi\rangle = \sum C_{d_1...d_i...d_n} |d_1...d_{\delta^v(k)}...d_k...d_{q+\delta^s(j)}...d_{q+j}...d_n\rangle \\
&CK(\theta_{jk})_{q+j,k} SWAP'|\psi\rangle = \sum C_{d_1...d_i...d_n} ((|d_1\rangle \otimes ... \otimes \mathbf{0} d_{q+\delta^s(j)} \otimes ... \otimes |d_{q+j}\rangle \otimes ... \otimes |d_\pi(n)\rangle) \\
&+ (|d_1\rangle \otimes ... \otimes K(\theta_{jk})|d_{\delta^v(k)}\rangle \otimes ... \otimes |d_k\rangle \otimes ... \otimes \mathbf{1}|d_{q+\delta^s(j)}\rangle \otimes ... \otimes |d_{q+j}\rangle \otimes ... \otimes |d_\pi(n)\rangle, \\
&SWAP'^T CK(\theta_{jk})_{q+j,k} SWAP'|\psi\rangle = \sum C_{d_1...d_i...d_n} ((|d_1\rangle \otimes ... \otimes d_{q+j} \otimes ... \otimes \mathbf{0}|d_{q+\delta^s(j)}\rangle \otimes \\
&... \otimes |d_\pi(n)\rangle) + (|d_1\rangle \otimes ... \otimes |d_k\rangle \otimes ... \otimes K(\theta_{jk})|d_{\delta^v(k)}\rangle \otimes ... \otimes |d_{q+j}\rangle \otimes ... \otimes \mathbf{1}|d_{q+\delta^s(j)}\rangle \otimes ... \otimes |d_\pi(n)\rangle, \\
&= CK(A_{jk} + \beta_t)_{q+\delta^s(j),\delta^v(k)} . |\psi\rangle
\end{aligned} \tag{14}$$

Therefore, we can obtain

$$SWAP'^T CK(A_{jk} + \beta_t)_{q+j,k} SWAP'|\psi\rangle = CK(A_{jk} + \beta_t)_{q+\delta^s(j),\delta^v(k)} = CK(A_{\delta^s(j')\delta^v(k')} + \beta_t)_{q+j',k'}, \tag{15}$$

where $j = \delta^s(j')$ and $k = \delta^v(k')$. It is known that $U_K^V(A, \beta) = \prod_{(j,k)\in\mathcal{E}} CK(A_{jk} + \beta_t)_{q+j,k}$

$$\begin{aligned}
SWAP'^T U_K^V(A, \beta_t) SWAP' &= \prod_{(j,k)\in\mathcal{E}} SWAP'^T CK(A_{jk} + \beta_t)_{q+j,k} SWAP' \\
&= \prod_{(j,k)\in\mathcal{E}} CK(A_{\delta^s(j')\delta^v(k')} + \beta_t)_{q+j',k'} = \prod_{(j',k')\in\mathcal{E}'} CK(A'_{\delta^s(j)\delta^v(k)} + \beta_t)_{q+j,k} \\
&= U_K^V(A', \beta_t) = U_K^V(\Lambda_{\delta_s} A \Lambda_{\delta_v}, \beta_t),
\end{aligned} \tag{16}$$

where Λ_{δ_s} and Λ_{δ_v} are the permutation matrices of the permutation δ_s and δ_v. The equation indicates the equivariance of the graph message interaction layer.

D.2.2 Proof of Theorem D.2

As mentioned earlier,

$$\Phi(A, H, \Theta) = \Phi(A, \mathrm{H^V}, \mathrm{H^S}, \Theta) = \{\langle 0|U_{peqg}^\dagger(A, \mathrm{H^V}, \mathrm{H^S}, \Theta) O_i U_{peqg}(A, \mathrm{H^V}, \mathrm{H^S}, \Theta)|0\rangle\}_{i=1}^{q+p}, \tag{17}$$

and we have proven that U_{peqg} is permutation equivariant. *i.e.*,

$$\widetilde{\Lambda}^\dagger \cdot U_{peqg}(A, \mathrm{H^V}, \mathrm{H^S}, \Theta) \cdot \widetilde{\Lambda} = U_{peqg}(\Lambda_p A \Lambda_q, \Lambda_q \mathrm{H^V}, \Lambda_p \mathrm{H^S}, \Theta). \tag{18}$$

Therefore, $\Phi(\Lambda_p A \Lambda_q, \Lambda_q \mathrm{H^V}, \Lambda_p \mathrm{H^S}, \Theta)$

$$\begin{aligned}
&= \{\langle 0|U_{peqg}^\dagger(\Lambda_p A \Lambda_q, \Lambda_q \mathrm{H^V}, \Lambda_p \mathrm{H^S}, \Theta) O_i U_{peqg}(\Lambda_p A \Lambda_q, \Lambda_q \mathrm{H^V}, \Lambda_p \mathrm{H^S}, \Theta)|0\rangle\}_{i=1}^{q+p} \\
&= \{\langle 0|\widetilde{\Lambda}^\dagger U_{peqg}^\dagger(A, \mathrm{H^V}, \mathrm{H^S}, \Theta))\widetilde{\Lambda} O_i \widetilde{\Lambda}^\dagger U_{peqg}(A, \mathrm{H^V}, \mathrm{H^S}, \Theta))\widetilde{\Lambda}|0\rangle\}_{i=1}^{q+p} \\
&= \{\langle 0|\widetilde{\Lambda}^\dagger U_{peqg}^\dagger(A, \mathrm{H^V}, \mathrm{H^S}, \Theta)) O_{\pi_{q+p}(i)} U_{peqg}(A, \mathrm{H^V}, \mathrm{H^S}, \Theta))\widetilde{\Lambda}|0\rangle\}_{i=1}^{q+p} \\
&= \Lambda_{q+p} \Phi(A, \mathrm{H^V}, \mathrm{H^S}, \Theta),
\end{aligned} \tag{19}$$

which indicates $\Phi(A, \mathrm{H_V}, \mathrm{H_S}, \Theta)$ is a permutation equivariant mapping.

D.2.3 Proof of Corollary D.1

Corollary D.3. ***(From Equivariance to Invariance).*** *If a mapping $\phi(A, H^V, H^S) \in \mathbb{R}^{q+p}$ is permutation equivariant, $\sum(\phi(A, H^V, H^S))$ is permutation invariant.*

Proof. Assume that $\phi(A, \mathrm{H}^{\mathrm{V}}, \mathrm{H}^{\mathrm{S}}) = [y_1, ..., y_{q+p}]^\top$, According to Definition 2, $\phi(\Lambda_p A \Lambda_q, \Lambda_q \mathrm{H}^{\mathrm{V}}, \Lambda_p \mathrm{H}^{\mathrm{S}}) = [y_{\pi_{q+p}(1)}, ..., y_{\pi_{q+p}(q+p)}]^\top$. Therefore, we can obtain $\sum(\phi(A, \mathrm{H}^{\mathrm{V}}, \mathrm{H}^{\mathrm{S}})) = \sum_{i=1}^{q+p} y_i = \sum_{i=1}^{q+p} y_{\pi_{q+p}(i)} = \sum(\phi(\Lambda_p A \Lambda_q, \Lambda_q \mathrm{H}^{\mathrm{V}}, \Lambda_p \mathrm{H}^{\mathrm{S}}))$.

By Theorem D.2 and Corollary D.3, we can obtain $\phi_{\text{fea}}(A, H) = \sum_{i=1}^{q+p} \Phi(A, H, \Theta_{fea})_i$ is permutation invariant. Similarly, the mapping of predicting objective value $\phi_{\text{obj}}(A, H) = \sum_{i=1}^{q+p} \Phi(A, H, \Theta_{obj})_i$ also holds.

D.2.4 An intuitive example of graph message interaction layers

In graph message interaction layers, each edge is mapped into a two-qubit quantum gate acted on qubits representing two nodes. For example, here is a graph G with three nodes a, b, c. After the first feature encoding layer, the quantum state $|\psi\rangle = |\psi_a\rangle \otimes |\psi_b\rangle \otimes |\psi_c\rangle$. If there is an edge connecting nodes a and b, the model will apply a two-qubit quantum gate between qubit q_a and qubit q_b. Suppose the used two-qubit gate is $R_{ZZ}(\theta) = \exp(-i\theta Z \otimes Z)$ gate, then it is equivalent to multiplying the quantum state by a matrix $U = R_{ZZ}(\theta) \otimes I$. Thus, the quantum state is changed as $|\psi'\rangle = U|\psi\rangle = (\exp(-i\theta Z \otimes Z) \otimes I)(|\psi_a\rangle \otimes |\psi_b\rangle \otimes |\psi_c\rangle) = (R_{ZZ}(\theta) \otimes I)(|\psi_{ab}\rangle \otimes |\psi_c\rangle) = |\psi'_{ab}\rangle \otimes |\psi_c\rangle$. In other words, the two-qubit gate alters the quantum states corresponding to nodes a and b, thereby achieving the goal of information exchange.

E VQGLA Can Distinguish MILP Graphs that GNN Cannot Distinguish

E.1 Why GNN Fails on the GNN-intractable MILPs

The discriminative power of GNN is defined as whether it can distinguish two non-isomorphic graphs. The representation power of GNN refers to its ability to approximate mappings with permutation equivariant/invariant properties. Moreover, Xu et al. (2018) have shown that GNNs are **at most** as powerful as the Weisfeiler-Lehman (WL) test Weisfeiler & Leman (1968) in distinguishing graph structures. The WL test is a well-known algorithm to identify whether two graphs are isomorphic or not, *i.e.*, whether two graphs are topologically identical. However, there are numerous WL test indistinguishable graphs, and the most well-known class is regular graphs, where every vertex has the same number of neighbors, *i.e.*, the same degree. According to the above, if a pair of graphs is indistinguishable by the WL test, GNN will also fail to distinguish them. In fact, the MILP graph dataset just contains numerous WL-indistinguishable graphs, so directly using GNN to represent general MILP graphs will lead to poor performance. Chen et al. (2023) extracted this subset of WL-indistinguishable graphs from the entire MILP dataset and named it the "GNN-intractable MILP". A variant of the WL test specially modified for MILP is provided in Algorithm 1. Based on the algorithm, it can intuitively show why the WL test cannot distinguish some non-isomorphic graphs, thereby showing why GNN cannot discriminate GNN-intractable MILPs.

Algorithm 1 WL test for MILP-Graphs

Input: A graph instance $(A, H) \in \mathcal{G}_{q,p} \times \mathcal{H}_q^V \times \mathcal{H}_p^S$, and iteration limit $L > 0$.
Initialize with $c_v^0 = hash(f^V)$ for all $v \in V$, $c_s^0 = hash(f^S)$ for all $s \in S$.
for $l = 1$ **to** L **do**
  $c_{v_i}^l = hash(c_{v_i}^{l-1}, \sum_{j=0}^{p-1} A_{i,j} hash(c_{s_j}^{l-1}))$, for all $v \in V$.
  $c_{s_j}^l = hash(c_{s_j}^{l-1}, \sum_{i=0}^{q-1} A_{i,j} hash(c_{v_i}^{l-1}))$, for all $s \in S$.
end for
Output: The multisets contain all colors $\{\{c_v^l : v \in V, c_s^l : s \in S\}\}$.

In the algorithm, $hash(\cdot)$ is a function that maps its input feature to a color in $\mathcal{C}$. The algorithm flow can be seen as follows. First, all nodes in $V \sup S$ are assigned to an initial color c_v^0 and c_s^0 according to their node features. Then, for each $v_i \in V$, the $hash$ function maps the previous color $c_{v_i}^{l-1}$ and aggregates the color of the neighbors of $\{c_{s_j}^{l-1}\}_{s_j \in \mathcal{N}(v_i)}$. Similarly, the $hash$ function maps

the previous color $c_{s_j}^{l-1}$ and aggregates the color of the neighbors of $\{c_{v_i}^{l-1}\}_{v_i \in \mathcal{N}(s_j)}$. This process is repeated until L reaches the maximum iteration number. Finally, a histogram h_G of the node colors can be obtained according to $\{\{c_v^l : v \in V, c_s^l : s \in S\}\}$, which can be used as a canonical graph representation. The notation $\{\{\cdot\}\}$ denotes a multiset, which is a generalisation of the concept of a set in which elements may appear multiple times. That is, the -WL test transforms a graph into a canonical representation. If the canonical representation of two graphs is equal, the WL test will consider them isomorphic.

Assume that there are two n-regular MILP graphs $G_1 = (A_1, H_1)$ and $G_2 = (A_2, H_2)$, where each node has n neighbors in both graphs. And we set $A1 \neq A_2$ and $H_1 = H_2$, *i.e.*, they have the same features but different topology structures (the connectivity of edges). For clarity, we set $\{f_i^V\}_{i=1}^q$ is the same, and $\{f_i^S\}_{j=1}^p$is the same. Fig. 1 is an example of this type of graph. Initially, in the WL-test, $(c_v^0)_{g1} = (c_v^0)_{g2}$ and $(c_s^0)_{g1} = (c_s^0)_{g2}$. Then, the representation of each vertex is updated iteratively based on itself and information from its neighbors. In both graphs, each variable node has the same number of constraint nodes, and all constraint features are the same, so all $c_{v_i}^l$ are identical at this step. Similarly, each constraint node has the same number of variable nodes, so all $c_{s_j}^l$ are identical. Until the maximum number of iterations is reached, the algorithm will output the same representation for these two graphs. Therefore, the WL-test or GNNs cannot distinguish them.

E.2 Proof of the Discriminative Power of VQGLA Better than GNNs

Theorem E.1. *VQGLA can capture the difference in edge connectivity between two MILP graphs.*

Proof. Suppose that $G_1 = (A_1, H_1)$ and $G_2 = (A_2, H_2)$, and the two graphs have only different edge connectivity or edge weights, *i.e.*, $A_1 \neq A_2$. In VQGLA, the layer related to A is the graph message interaction layer. As shown in Eq. 8, the sublayers related to A are U_K layers. All U_K layers have similar structures. For clarity, we consider the following a simplified U_K layer (where one qubit represents one node) to showcase how VQGLA captures the topological structure. *i.e.*,

$$U_K^V(A) = \exp(-\mathbf{i}(\sum_{(i,j)\in\mathcal{E}} A_{i,j}(I-\sigma_z)_i P_{q+j}^K)).$$

Note that $i \in \{1, ..., q\}$ and $j \in \{1, ..., p\}$, and $(I - \sigma_z)_i$ is equal to $\underbrace{I \otimes ... \otimes ...}_{i-1} \otimes (I - \sigma_z) \otimes \underbrace{... \otimes I}_{q-i} \otimes \underbrace{... \otimes I}_{p}$. Similarly, $P_{q+j}^K = \underbrace{I \otimes ... \otimes I}_{q} \underbrace{\otimes ... \otimes}_{j-1} P^K \underbrace{\otimes ... \otimes I}_{p-j}$. Therefore, $(I - \sigma_z)_i P_{q+j}^K = \underbrace{I \otimes ... \otimes}_{i-1} (I - \sigma_z) \underbrace{\otimes ... \otimes I}_{q-i} \underbrace{\otimes ... \otimes}_{j-1} P^K \underbrace{\otimes ... \otimes I}_{p-j}$.

As we can see, for $(I-\sigma_z)_i P_{q+j}^K$, $I-\sigma_z$ appears in one of the first q positions, and P^K is acted in one of the last p positions. For different edges, $(I - \sigma_z)_i P_{q+j}^K$ is different. More importantly, for different edge sets, $\sum_{(i,j)\in\mathcal{E}} A_{i,j}(I - \sigma_z)_i P_{q+j}^K$ is also different due to the properties of tensor products. Therefore, if $A_1 \neq A_2$, resulting in $U_K^V(A_1) \neq U_K^V(A_2)$, which indicates the VQGLA can capture the difference in edge connectivity between two MILP graphs. Although two non-isomorphic regular graphs have the same degree, the edge connectivity is different. That is, VQGLA can distinguish GNN-intractable MILP graphs that GNN fails to distinguish.

F The Performance of All Possible Types of VQGLAs

Table 11 lists all possible selections of the quantum gate in VQGLA. The type represents (P^w, P^D, P^K, P^G). For example, when the type is equal to $(\sigma_x, \sigma_z, \sigma_y, \sigma_z)$, it indicates $W(\theta) = R_X(\theta)$, $D(\theta) = R_Z(\theta)$, $CK(\theta) = CR_Y(\theta)$, and $G(\theta) = R_Z(\theta)$. To compare the performance of different settings, we test them on the task of predicting the feasibility of the GNN-tractable MILP dataset. In the experiment, we set the block of VQGLA is 8, the number of epochs to 15, the learning rate to 0.1, and the batch size to 16. Table 11 shows VQGLA with $(\sigma_x, \sigma_z, \sigma_y, \sigma_z)$ can achieve the best result, so we adopt this scheme in our all experiments.

Table 11: All possible selections of VQGLA and their performance results on predicting the feasibility of GNN-tractable MILP datasets. Results demonstrated that $(\sigma_x, \sigma_z, \sigma_y, \sigma_z)$ can achieve the best performance.

Types	$(\sigma_x, \sigma_y, \sigma_z, \sigma_y)$	$(\sigma_x, \sigma_z, \sigma_y, \sigma_z)$	$(\sigma_y, \sigma_x, \sigma_z, \sigma_x)$	$(\sigma_y, \sigma_z, \sigma_x, \sigma_z)$	$(\sigma_z, \sigma_x, \sigma_y, \sigma_x)$	$(\sigma_z, \sigma_y, \sigma_x, \sigma_y)$
Train	0.0598	0.0557	0.0724	0.0623	0.0635	0.0615
Test	0.0606	0.0574	0.0741	0.0625	0.0647	0.0635

G MILP Dataset Generation

For GNN-tractable MILPs, we first set the number of variables and constraints to m and n.

- For each variable, $c_j \sim \mathcal{N}(0, 0.01)$, $l_j, u_j \sim \mathcal{U}(0, 2\pi)$. If $l_j > u_j$, then switch l_j and u_j. The probability that x_j is an integer variable is 0.5.
- For each constraint, $\circ_i \sim \mathcal{U}(\leq, =, \geq)$ and $b_i \sim \mathcal{U}(-1, 1)$.
- After randomly generating all the MILP samples, we use the WL test algorithm to calculate their graph representation for each instance, ensuring that there are no duplicate graph representations in the dataset, so that we can determine that this dataset does not contain WL-test indistinguishable pairs of MILP instances.

The GNN-intractable dataset is constructed by many pairs of WL indistinguishable graphs, and Fig. 1 in our paper is a GNN-intractable example, which is a pair of non-isomorphic graphs that cannot be distinguished by the WL-test or by GNNs. The GNN-intractable dataset randomly generates 2000 GNN-intractable MILPs with 12 variables and 6 constraints, and there are 1000 feasible MILPs with feasible optimal solutions while the others are infeasible. We construct the $(2k-1)$-th and $2k$-th problems via the following approach, where $(1 \leq k \leq 500)$.

- Sample $J = \{j_1, j_2, ..., j_6\}$ as a random subset of $\{1, 2, ..., 12\}$ with 6 elements. **1)** For $j \in J$, $x_j \in \{0, 1\}$, i.e., x_j is a binary integer variable. **2)** For $j \notin J$, x_j is a continuous variable with bounds $l_j \sim \mathcal{U}(0, \pi)$, $u_j \sim \mathcal{U}(0, \pi)$. If $l_j > u_j$, then switch l_j and u_j.
- $c_1 = ... = c_{12} = 0.01$.
- The constraints for the $(2k-1)$-th problem (feasible) is $x_{j_1} + x_{j_2} = 1$, $x_{j_2} + x_{j_3} = 1$, $x_{j_3} + x_{j_4} = 1$, $x_{j_4} + x_{j_5} = 1$, $x_{j_5} + x_{j_6} = 1$, $x_{j_6} + x_{j_1} = 1$. For example, $x = (0, 1, 0, 1, 0, 1)$ is a feasible solution.
- The constraints for the $2k$-th problem (infeasible) is $x_{j_1} + x_{j_2} = 1$, $x_{j_2} + x_{j_3} = 1$, $x_{j_3} + x_{j_1} = 1$, $x_{j_4} + x_{j_5} = 1$, $x_{j_5} + x_{j_6} = 1$, $x_{j_6} + x_{j_4} = 1$.

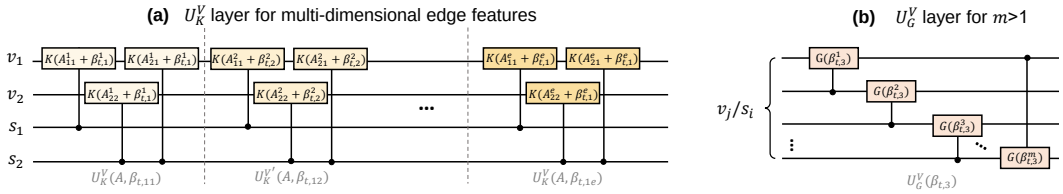

Figure 9: (a) The controlled K layer for multi-dimensional edge features. (b) The controlled G layer for $m > 1$, where m is the number of qubits representing one node v_j or s_i.

H The Capacity of VQGLA

The proposed framework can also be used for situations where the edge dimension is more than one. As shown in Fig. 9 (a), the controlled K gates can be repeatedly applied with different edge dimensions. In addition, Fig. 9 (b) illustrates the detailed circuit when the number of qubits representing one node is more than one. Moreover, although VQGLA is designed for MILP graphs, i.e., bipartite graphs, it can be easily extended to arbitrary graphs. Specifically, in the quantum graph message interaction layer, we can apply symmetric two-qubit gates, such as R_{ZZ} gate, between two nodes, representing edges in an arbitrary graph and preserving the edge permutation invariance. The remaining structure can remain completely unchanged when applied to an arbitrary graph.

It has been shown that general QNNs may suffer from barren plateau (McClean et al., 2018), *i.e.*, the loss gradients vanish exponentially with the system size, causing the trainability of QNNs becomes an important issue. However, Fig. 10 shows the variance of our cost function partial derivatives for a parameter in the middle of VQGLA. The variance only decreases polynomially with the system size, which shows that VQGLA has good trainability.

Figure 10: Variance v.s qubits (log-linear scale).

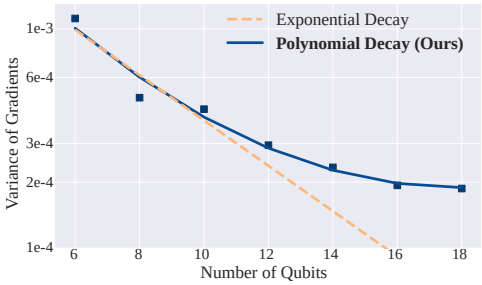

I THE DETAILS OF U_K LAYER

In the training process, the types (e.g., $RX(\theta)$, $RY(\theta)$, or $RZ(\theta)$) and positions of gates are fixed, but their internal parameters are not fixed in the quantum machine learning. Therefore, it should be noted that when implementing the proposed graph message interaction layer, there is actually a controlled K gate between each variable node and each constraint node (like a fully connected bipartite graph). However, if there is no edge between the two nodes, we will set the parameters of the corresponding controlled K gate to 0. $CK(0)$ is an identity matrix that will not affect the overall circuit. Specifically, in code engineering, we first obtain the binary adjacency matrix T of the bipartite graph. $T_{ij} = 1$ indicates that there is an edge connecting constraint node s_i and variable node v_j, while $T_{ij} = 0$ indicates that there is no edge connecting them. Then, $CK(T_{ij}(A_{ij} + \beta))$ is acted on the two qubits representing constraint node s_i and variable node v_j. As we can see, when there is an edge between the two qubits, $CK(A_{ij} + \beta)$ is acted on the two qubits, while when there is no edge between the two qubits, $CK(0)$ is acted on the two qubits. In this way, we can achieve the modeling of the graph message interaction layer under the premise of fixed gate types and positions.

J THE IMPLEMENTATION ON REAL QUANTUM DEVICES

Thanks for your suggestions. Our proposed VQGLA quantum circuit consists of only simple single-qubit and two-qubit gates, making it easy to deploy on existing NISQ devices. To verify this, we use the Qiskit package and the IBM Quantum platform to directly execute our circuits on real IBM quantum hardware. The circuits are first compiled and optimized, then mapped to the real quantum hardware's topology using the $generate_preset_pass_manager$ function. Subsequently, the expectation values of the quantum circuits are estimated using the *Estimator V2* primitive. The Estimator primitive supports three resilience levels: Resilience Level 0 represents no error mitigation techniques are applied. Resilience Level 1 applies readout error mitigation and measurement twirling using a model-free technique known as Twirled Readout Error eXtinction (TREX) (Van Den Berg et al., 2022). Resilience Level 2 includes the error mitigation techniques from Level 1 and further applies gate twirling and the Zero Noise Extrapolation (ZNE) (Temme et al., 2017).

We conducted experiments using 10 minutes of free usage on the 127-qubit *IBM Brisbane* quantum computer, and evaluate the mean square error (MSE) compared to ground truth on MILP dataset with three different scales, as shown in the table below.

	18 qubit	26 qubit	36 qubit
Noise (ibm_brisbane)	0.2627	0.2850	0.3461
resilience_level = 1	0.2107	0.2428	0.3336
resilience_level = 2	0.2077	0.2174	0.3176

Table 12: Performance comparison across different qubit numbers and resilience levels.

The results demonstrate that employing error mitigation strategies can improve performance. Higher resilience levels produce more accurate results, but at the cost of increased processing time, which is a trade-off between cost and accuracy.